

1 **Title:**

2 The Coupling Cloud: A community database of megathrust kinematic coupling models

3 **Authors:**

4 Bar Oryan<sup>1</sup>, Alice-Agnes Gabriel<sup>1+2</sup>, Roland Bürgmann<sup>3</sup>, Eric Calais<sup>4</sup>, Guo Cheng<sup>5</sup>, Mohamed  
5 Chlieh<sup>6</sup>, Beatriz Cosenza-Murallas<sup>7</sup>, Víctor M. Cruz-Atienza<sup>8</sup>, Luca Dal Zilio<sup>9+10</sup>, Charles DeMets<sup>11</sup>,  
6 Andria Ellis<sup>12</sup>, Lujia Feng<sup>9+10</sup>, Jeffrey T. Freymueller<sup>13</sup>, Endra Gunawan<sup>14</sup>, Nuraini R. Hanifa<sup>15</sup>,  
7 George E. Hilley<sup>16</sup>, Ya-Ju Hsu<sup>17</sup>, Takeshi Iinuma<sup>18</sup>, Yuji Itoh<sup>19</sup>, Jorge Jara<sup>20</sup>, Kaj M. Johnson<sup>21</sup>, Romain  
8 Jolivet<sup>4+22</sup>, Masayuki Kano<sup>23</sup>, Emilie Klein<sup>4</sup>, Shanshan Li<sup>24</sup>, Shaoyang Li<sup>25</sup>, Eric O. Lindsey<sup>26</sup>, Zhen  
9 Liu<sup>27</sup>, John P. Loveless<sup>28</sup>, Bertrand Løvery<sup>6</sup>, Louise Maubant<sup>19</sup>, Sylvain Michel<sup>29+30</sup>, Cyril Muller<sup>31</sup>,  
10 Marianne Métois<sup>32</sup>, Takuya Nishimura<sup>23</sup>, Akemi Noda<sup>33</sup>, Dibyashakti Panda<sup>34</sup>, Mason Perry<sup>9</sup>,  
11 Raymundo Plata-Martinez<sup>8</sup>, Mathilde Radiguet<sup>6</sup>, Baptiste Rousset<sup>35</sup>, Elizabeth M. Sherrill<sup>36</sup>, Anne  
12 Socquet<sup>6</sup>, Juan Carlos Villegas-Lanza<sup>37</sup>, Laura M. Wallace<sup>36+38</sup>, Lian Xue<sup>39</sup>, Yusuke Yokota<sup>40</sup>,  
13 Shoichi Yoshioka<sup>41+42</sup> and Shui-Beih Yu<sup>17</sup>

14

15 (1) Scripps Institution of Oceanography, University of California at San Diego, La Jolla, CA 92093,  
16 USA

17 (2) Department of Earth and Environmental Sciences, Ludwig-Maximilians-University, 80333  
18 Munich, Germany

19 (3) Department of Earth and Planetary Science, UC Berkeley

20 (4) Laboratoire de Géologie, Ecole normale supérieure - PSL, CNRS UMR 8538, Paris France

21 (5) Nevada Bureau of Mines and Geology, University of Nevada, Reno, NV, USA

22 (6) Univ. Grenoble Alpes, Univ. Savoie Mont Blanc, CNRS, IRD, Univ. Gustave Eiffel, STerre, 38000  
23 Grenoble, France

24 (7) Instituto de Investigación en Ciencias Físicas y Matemáticas (IFIM), Escuela de Ciencias Físicas  
25 y Matemáticas, Universidad de San Carlos de Guatemala

26 (8) Instituto de Geofísica, Universidad Nacional Autónoma de México

27 (9) Earth Observatory of Singapore, Nanyang Technological University, Singapore, Singapore

28 (10) Asian School of the Environment, Nanyang Technological University, Singapore, Singapore

29 (11) Department of Geoscience, University of Wisconsin-Madison, Madison WI 53706 USA

30 (12) Department of Earth and Environmental Sciences, Michigan State University, East Lansing,  
31 MI, USA

32 (13) USGS Hawaiian Volcano Observatory

33 (14) Institut Teknologi Bandung, Indonesia

34 (15) Research Center for Geological Disaster, National Research and Innovation Agency, Bandung,  
35 Indonesia

- 36 (16) Stanford University, Stanford, CA, USA  
37 (17) Institute of Earth Sciences, Academia Sinica  
38 (18) Japan Agency for Marine-Earth Science and Technology, Yokohama, Japan  
39 (19) Earthquake Research Institute, The University of Tokyo, Tokyo, Japan  
40 (20) GFZ Helmholtz Centre for Geosciences, Potsdam, Germany  
41 (21) Department of Earth and Atmospheric Sciences, Indiana University, Bloomington, IN, USA  
42 (22) Institut Universitaire de France, 1 rue Descartes, 75006 Paris, France  
43 (23) Disaster Prevention Research Institute, Kyoto University, Japan  
44 (24) School of Computing at University of Wyoming  
45 (25) State Key Laboratory of Lithospheric and Environmental Coevolution, Institute of Geology  
46 and Geophysics, Chinese Academy of Sciences, Beijing, China  
47 (26) Department of Earth & Planetary Sciences, University of New Mexico, Albuquerque, NM,  
48 USA  
49 (27) Jet Propulsion Laboratory, California Institute of Technology  
50 (28) Department of Geosciences, Smith College, Northampton, MA, USA  
51 (29) Université Côte d'Azur, IRD, CNRS, Observatoire de la Côte d'Azur, Valbonne, France  
52 (30) Sorbonne Université, CNRS-INSU, Institut des Sciences de la Terre Paris, ISTeP UMR 7193,  
53 Paris, France  
54 (31) Observatorio Vulcanológico y Sismológico de Costa Rica, Universidad Nacional de Costa Rica  
55 Heredia, Costa Rica  
56 (32) Université Claude Bernard Lyon 1, ENS de Lyon, Université Jean Monnet, CNRS, LGL-TPE,  
57 UMR5276  
58 (33) National Institute of Advanced Industrial Science and Technology, Tsukuba, Japan.  
59 (34) Department of Geology, School of Earth Sciences, Central University of Tamil Nadu,  
60 Thiruvavur, India, 610005  
61 (35) Institut Terre et Environnement de Strasbourg UMR7063, Université de  
62 Strasbourg/CNRS/ENGESS, 5 Rue René Descartes, Strasbourg, 67000, France  
63 (36) GEOMAR Helmholtz Centre for Ocean Research Kiel, Germany  
64 (37) Instituto Geofísico del Perú (IGP), Lima, Peru  
65 (38) Institute for Geophysics, University of Texas, Austin, TX, USA  
66 (39) School of Earth and Space Science, Peking University, Beijing, China  
67 (40) Institute of Industrial Science, University of Tokyo, Japan  
68 (41) Research Center for Urban Safety and Security, Kobe University, Rokkodai-cho 1-1, Nada  
69 ward, Kobe 657-8501, Japan  
70 (42) Department of Planetology, Graduate School of Science, Kobe University, Rokkodai-cho 1-1,  
71 Nada ward, Kobe 657-8501, Japan

## 72 Author ORCIDs

- 73 Bar Oryan:0000-0001-5000-5668
- 74 Alice-Agnes Gabriel:0000-0003-0112-8412
- 75 Roland Bürgmann:0000-0002-3560-044X
- 76 Eric Calais:0000-0002-5935-8117
- 77 Guo Cheng:0000-0002-4144-8448
- 78 Mohamed Chlieh:0000-0003-2252-2187
- 79 Beatriz Cosenza-Murallas:0000-0002-4626-2757
- 80 Víctor M. Cruz-Atienza:0000-0001-7067-2636
- 81 Luca Dal Zilio:0000-0002-5642-0894
- 82 Charles DeMets:0000-0001-7460-1165
- 83 Andria Ellis:0000-0003-2543-0640
- 84 Lujia Feng:0000-0002-3736-5025
- 85 Jeffrey T. Freymueller:0000-0003-0614-0306
- 86 Endra Gunawan:0000-0002-7187-1466
- 87 Nuraini R. Hanifa:0000-0002-8012-5385
- 88 George E. Hilley:0000-0002-1761-7547
- 89 Ya-Ju Hsu:0000-0003-1389-9994
- 90 Takeshi Inuma:0000-0003-0386-2055
- 91 Yuji Itoh:0000-0002-7848-1399
- 92 Jorge Jara:0000-0003-3176-0689
- 93 Kaj M. Johnson:0000-0003-1511-5241
- 94 Romain Jolivet:0000-0002-9896-3651
- 95 Masayuki Kano:0000-0002-7288-4760
- 96 Emilie Klein:0000-0003-3239-5118
- 97 Shanshan Li:0000-0002-8986-431X
- 98 Shaoyang Li:0000-0001-9832-4561
- 99 Eric O. Lindsey:0000-0003-2274-8215
- 100 Zhen Liu:0000-0002-6313-823X
- 101 John P. Loveless:0000-0003-0416-8727
- 102 Bertrand Lavery:0000-0002-3671-0608
- 103 Louise Maubant:0000-0003-2077-169X
- 104 Sylvain Michel:0000-0001-7878-6603
- 105 Cyril Muller:0000-0003-3744-5700
- 106 Marianne Métois:0000-0002-1489-0513
- 107 Takuya Nishimura:0000-0002-2469-8146

108 Akemi Noda:0000-0002-9825-568X  
109 Dibyashakti Panda:0000-0002-3190-9693  
110 Mason Perry:0000-0003-1719-9004  
111 Raymundo Plata-Martinez:0000-0001-9272-0926  
112 Mathilde Radiguet:0000-0002-3877-9393  
113 Baptiste Rousset:0000-0001-9304-0498  
114 Elizabeth M. Sherrill:0000-0002-5439-6464  
115 Anne Socquet:0000-0002-9208-7136  
116 Juan Carlos Villegas-Lanza:0000-0002-2772-1508  
117 Laura M. Wallace:0000-0003-2070-0891  
118 Lian Xue:0000-0002-0739-7616  
119 Yusuke Yokota:0000-0003-2969-9110  
120 Shoichi Yoshioka:0000-0002-0238-1033  
121 Shui-Beih Yu:0000-0002-1754-6208

## 122 Author contributions

123 Conceptualization: B. Oryan, A. Gabriel

124

125 Data Curation: B. Oryan, A. Gabriel, R. Bürgmann, E. Calais, G. Cheng, M. Chlieh, B. Cosenza-  
126 Muralles, V. Cruz-Atienza, L. Dal Zilio, C. DeMets, A. Ellis, L. Feng, J. Freymueller, E. Gunawan, N.  
127 Hanifa, G. Hilley, Y. Hsu, T. Iinuma, Y. Itoh, J. Jara, K. Johnson, R. Jolivet, M. Kano, E. Klein, S. Li, S.  
128 Li, E. Lindsey, Z. Liu, J. Loveless, B. Lavery, L. Maubant, S. Michel, C. Muller, M. Métois, T.  
129 Nishimura, A. Noda, D. Panda, M. Perry, R. Plata-Martinez, M. Radiguet, B. Rousset, E. Sherrill, A.  
130 Socquet, J. Villegas-Lanza, L. Wallace, L. Xue, Y. Yokota, S. Yoshioka, S. Yu

131

132 Validation: B. Oryan, A. Gabriel, R. Bürgmann, E. Calais, G. Cheng, M. Chlieh, B. Cosenza-Muralles,  
133 V. Cruz-Atienza, L. Dal Zilio, C. DeMets, A. Ellis, L. Feng, J. Freymueller, E. Gunawan, N. Hanifa, G.  
134 Hilley, Y. Hsu, T. Iinuma, Y. Itoh, J. Jara, K. Johnson, R. Jolivet, M. Kano, E. Klein, S. Li, S. Li, E.  
135 Lindsey, Z. Liu, J. Loveless, B. Lavery, L. Maubant, S. Michel, C. Muller, M. Métois, T. Nishimura,  
136 A. Noda, D. Panda, M. Perry, R. Plata-Martinez, M. Radiguet, B. Rousset, E. Sherrill, A. Socquet, J.  
137 Villegas-Lanza, L. Wallace, L. Xue, Y. Yokota, S. Yoshioka, S. Yu

138

139 Funding Acquisition: B. Oryan, A. Gabriel

140

141 Methodology: B. Oryan, A. Gabriel

142

143 Project Administration: B. Oryan, A. Gabriel

144

145 Software: B. Oryan

146  
147 Supervision: A. Gabriel  
148  
149 Visualization: B. Oryan  
150  
151 Writing – original draft: B. Oryan, A. Gabriel  
152  
153 Writing – review & editing: B. Lavery, Cyril Muller, Roland Bürgmann, Eric Calais, Jeffrey T.  
154 Freymueller, Marianne Métois, Víctor M. Cruz-Atienza, Takuya Nishimura, Emilie Klein, Charles  
155 DeMets, Dibyashakti Panda, Louise Maubant, Shoichi Yoshioka, Jorge Jara, Mathilde Radiguet,  
156 Sylvain Michel, Ya-Ju Hsu, Yuji Itoh, Lujia Feng, Shaoyang Li, Romain Jolivet, Jack Loveless, J.  
157 Villegas-Lanza, Yusuke Yokota, Mason Perry, Baptiste Rousset, Zhen Liu, Beatriz Cosenza-  
158 Muralles, Raymundo Plata-Martinez, N.R. Hanifa, Eric O. Lindsey, Elizabeth M. Sherrill  
159

## 160 Abstract

161 Kinematic coupling models inverted from geodetic data are widely used to evaluate how slip  
162 deficit is distributed along subduction megathrusts during the interseismic period, and are  
163 central to earthquake and tsunami hazard assessment. Yet, existing coupling models differ widely  
164 in methodology and inputs, lack common community standards, and are scattered across  
165 publications and repositories. Here, we introduce the “Coupling Cloud”  
166 (<https://couplingcloud.ucsd.edu>), an open, extensible, community-driven platform that curates,  
167 standardizes, documents, and disseminates more than 96 kinematic coupling models from 55  
168 publications across 21 subduction margins. The platform provides interactive 2D and 3D plate-  
169 interface viewers to inspect coupling models together with associated information such as slab  
170 geometry, uncertainty estimates and metadata. All datasets can be downloaded directly in  
171 standardized formats: surface-projected coupling values as NetCDF, plate-interface dislocation  
172 geometries as VTU, and model metadata as YAML files. We demonstrate the advantages of  
173 centralized and standardized coupling data through a Cascadia subduction zone example, where  
174 synthesizing eight full-margin models reveals along-strike patterns that are not apparent when  
175 models are examined individually. Consolidating coupling models within a coherent, version-  
176 controlled framework enables systematic cross-margin comparison and FAIR-compliant data  
177 sharing, opening the door to more comprehensive assessment of megathrust mechanics.

## 178 Introduction

179 Community databases can accelerate Earth science research by standardizing how data products  
180 are archived and shared, enabling synthesis across models and systematic evaluation of  
181 methodological choices. Several initiatives illustrate the scientific value of open, standardized  
182 data infrastructures. For example, SubMachine compiles global seismic tomography models  
183 (Hosseini et al., 2018), the SubMap initiative assembles long-term subduction zone observations  
184 (<https://submap.gm.umontpellier.fr/>), and the Nevada Geodetic Laboratory provides processed  
185 GNSS time series and velocity fields (Blewitt et al., 2018). Similarly, the SRCMOD database unified  
186 finite-fault source inversion formats and metadata to aggregate hundreds of finite slip models  
187 (Mai & Thingbaijam, 2014), directly motivating community benchmarks such as the Source  
188 Inversion Validation exercises (SIV, Mai et al., 2016). The USGS finite-fault model archive provides  
189 another example of how openly accessible, consistently formatted datasets accelerate scientific  
190 discovery (Goldberg et al., 2022; Hayes, 2017; <https://earthquake.usgs.gov/data/finitefault/>). In  
191 contrast, despite the central role of coupling models in subduction zone science and hazard  
192 assessment, the geodetic megathrust coupling community has lacked a centralized, standardized  
193 infrastructure for archiving, comparing, and reusing published models in consistent,  
194 interoperable data formats.

195 Kinematic coupling models identify regions along subduction interfaces that accommodate little  
196 interseismic slip, commonly inferred as frictionally locked, amid regions that creep steadily or slip  
197 transiently during the interseismic period. These models are constructed from inversions of  
198 interseismic or inter-slow slip events (inter-SSE) surface displacements most commonly derived  
199 from GNSS (Dixon, 1991; Feigl et al., 1993) and InSAR (Bürgmann et al., 2000), but also  
200 incorporating leveling (Burgette et al., 2009; Jackson & Bilham, 1994), coral-based  
201 reconstructions (Chlieh et al., 2008; Tsang et al., 2015) and offshore geodetic measurements such  
202 as GNSS-Acoustic techniques (DeSanto et al., 2025; Gagnon et al., 2005; Yokota et al., 2016). Such  
203 inversions commonly use Green's functions from forward models based on elastic dislocation  
204 theory in a half-space (Meade, 2007; Okada, 1985, 1992), or viscoelastic earthquake-cycle  
205 formulations (Itoh et al., 2021; Li et al., 2015, 2018; Pollitz, 1997) and the backslip formulation to  
206 infer slip deficit (Savage, 1983). The inverse problem is then solved with linear schemes  
207 (Tarantola, 2005; Tarantola & Valette, 1982) or Bayesian approaches that integrate priors with  
208 data to quantify posterior uncertainty (e.g., Fukuda & Johnson, 2008; Minson et al., 2013; Tomita  
209 et al., 2021; Yabuki & Matsu'ura, 1992). Expressing the inferred slip deficit rate relative to the  
210 long-term plate convergence rate yields a kinematic coupling model (Wang & Dixon, 2004) that  
211 describes a continuous spectrum of fault behavior, ranging from areas creeping at the long-term  
212 slip rate (coupling  $\approx 0$ ) to effectively fixed regions with no creep (coupling  $\approx 1$ ).

213 Because kinematic coupling models delineate regions where elastic strain accumulates and may  
214 be released in future megathrust earthquakes, they are an important tool for assessing seismic  
215 and tsunami hazard in subduction zones (e.g., Giardini et al., 1999; Glehman et al., 2025; Ramos  
216 et al., 2021; Small & Melgar, 2021; Wang et al., 2015; Wang, 2011; Widiyantoro et al., 2020).  
217 However, despite their scientific value, these models face methodological challenges. Differences  
218 in assumed slab geometry and viscoelastic earth structure (Laske et al., 2013; Loversy et al., 2025;  
219 Luo et al., 2025; Wang et al., 2021), the period studied, density and quality of geodetic  
220 observations, velocity plate model, and the imposed regularization applied during coupling  
221 inversion affect the resulting coupling distributions (Fukuda & Johnson, 2008; Ide, 2007; Minson  
222 et al., 2013). Moreover, kinematic coupling models have traditionally lacked a unified, FAIR-  
223 compliant (Findable, Accessible, Interoperable, Reusable; Wilkinson et al., 2016) data format and  
224 are often scattered across publications in forms that are difficult to extract, evaluate, or  
225 systematically compare, limiting reproducibility and efforts to assess how modeling assumptions  
226 affect coupling estimates.

227 Here, we present the Coupling Cloud (<https://couplingcloud.ucsd.edu>, hereafter abbreviated to  
228 CC), an open online platform that aggregates a growing collection of published kinematic  
229 coupling models from subduction zones worldwide. The CC provides an intuitive interface to  
230 explore, visualize, and download these version controlled models, featuring a 2D map viewer for  
231 surface-projected coupling values and a 3D viewer that displays coupling on the underlying slab  
232 geometry. By centralizing and unifying these datasets and providing both 2D and 3D visualization  
233 tools within a single platform, the CC facilitates comparative analysis, strengthens reproducibility,  
234 and broadens community access to essential megathrust earthquake science resources. We  
235 demonstrate the value of this unified framework with a Cascadia case study, where along-strike  
236 patterns emerging from averaged models are not apparent when models are examined  
237 individually.

## 238 Data selection

239 As of January 12, 2026 the CC database comprises 96 kinematic coupling datasets compiled from  
240 55 publications covering 21 subduction zones worldwide, for a total of 219 spatial data products.  
241 These represent all published coupling models for which datasets were available and that use  
242 geodetic observations to infer the spatial distribution of coupling along subduction megathrusts.  
243 The database currently includes (in alphabetical order) two models in Alaska and the Aleutians  
244 (Drooff & Freymueller, 2021; Shanshan Li & Freymueller, 2018), two in the Caribbean (van  
245 Rijnsingen et al., 2021), eleven in Cascadia (Li et al., 2018; Lindsey et al., 2021; Materna et al., 2023;  
246 Michel et al., 2019; Pollitz & Evans, 2017; Pollitz, 2025; Schmalzle et al., 2014; Sherrill et al., 2024),

247 eight in Chile (Jara et al., 2024; Jolivet et al., 2020; Klein et al., 2018; Li et al., 2015; Métois et al.,  
248 2012, 2013, 2016), four in Costa Rica (Feng et al., 2012; Perry et al., 2025; Xue et al., 2015), two  
249 in Ecuador-Colombia (Chlieh et al., 2021; Gombert et al., 2018), one in Guatemala (Ellis et al.,  
250 2019), six in Hikurangi (Maubant et al., 2023; Michel et al., 2025; Wallace et al., 2012, three in  
251 Himalayas (Dal Zilio et al., 2020; Panda & Lindsey, 2024; Stevens & Avouac, 2015), one in Indo-  
252 Burma (Lindsey et al., 2023), nineteen in the Japan Trench (Abe & Yoshioka, 2022; Itoh et al.,  
253 2021; Lindsey et al., 2021; Loveless & Meade, 2016), two in Java (Hanifa et al., 2014; Widiyantoro  
254 et al., 2020), four in Kamchatka (Bürgmann et al., 2005), two in Manila (Hsu et al., 2016), two in  
255 Makran (Cheng et al., 2024), six in Mexico (Cosenza-Muralles et al., 2022; Cruz-Atienza et al.,  
256 2025; Louise Maubant et al., 2022; Radiguet et al., 2016; Rousset et al., 2016), nine in Nankai (Liu  
257 et al., 2010; Loveless & Meade, 2016; Nishimura et al., 2018; Noda et al., 2018; Plata-Martinez et  
258 al., 2024; Sherrill et al., 2024; Yokota et al., 2016), ten in Peru (Jara et al., 2024; Lovery et al.,  
259 2024; Villegas-Lanza et al., 2016), one in Ryukyu (Kano et al., 2021), three in the Sagami trough  
260 (Loveless & Meade, 2016; Nishimura et al., 2018), and one in Sumatra (Chlieh et al., 2008). While  
261 the Coupling Cloud provides standardized access to these datasets, users are expected to cite the  
262 original publications associated with each model when using the data.

## 263 Data standardization and unified representation

264 Published coupling models vary widely in format and metadata, reflecting the diversity of data  
265 coverage, methods, and conventions used across studies and time. To standardize access and  
266 promote FAIR use (Wilkinson et al., 2016), we map each model onto a uniform latitude–longitude  
267 grid and store it as a NetCDF file (Rew & Davis, 1990). When gridded outputs are not provided,  
268 coupling fields are interpolated onto a regular grid with adaptively refined resolution using linear  
269 or triangular interpolation (Text S1, Fig. S1). Every file contains latitude, longitude, the coupling  
270 values, and additional optional parameters, such as standard deviation, interface depth, and slip  
271 deficit. The NetCDF format is machine-readable and supports direct analyses and visualization  
272 using open-source packages such as Matplotlib (Hunter, 2007), GMT (Wessel et al., 2019), and  
273 Xarray (Hoyer & Hamman, 2017). Because NetCDF files do not inherently preserve the original  
274 fault-dislocation geometry used to invert the geodetic observations, we reformat all available  
275 model dislocation geometries as VTU PolyData files (Schroeder et al., 1998). VTU is a widely  
276 adopted, self-describing format for unstructured meshes that natively supports complex 3D slab  
277 geometries and mixed element types, making it well suited for downstream use in numerical  
278 modeling workflows. This standardized format allows for direct visualization and processing using  
279 open-source tools such as ParaView (Ahrens et al., 2005), PyVista (Sullivan & Kaszynski, 2019),  
280 and Meshio (Schlömer, 2022) and preserves node coordinates, mesh connectivity, and associated  
281 attributes such as coupling values on both node and element levels. Together, these machine-

282 readable formats remove the need to parse ASCII text files and allow users to work directly with  
283 the models using the tools listed above. They allow for quantitative operations, e.g., clipping by  
284 depth, computing isosurfaces, resampling to regular grids, decimation, and provide efficient  
285 binary input/output (I/O) with compression for large models. Both the regular-grid NetCDF  
286 products and the unstructured VTU meshes integrate with standard parallel analysis and  
287 visualization tools used in high-performance computing (HPC) workflows, enabling future  
288 scalable processing of large coupling model ensembles.

289 Beyond the spatial formats, we collect metadata on each study's modeling choices and  
290 assumptions to provide context for every hosted coupling model. Each dataset includes metadata  
291 detailing the source publication DOI, allowing users to readily identify and cite the original  
292 studies, as well as a short description, region, and model type. The latter distinguishes between  
293 interseismic coupling models that represent time-averaged strain accumulation between  
294 earthquakes, inter-SSE models estimated during periods between slow-slip events, and kinematic  
295 block-model formulations that infer coupling from relative motions between tectonic blocks.  
296 Additional optional metadata includes the quantity and type of geodetic observations, the  
297 forward model formulation, and the inversion framework, including parameters such as the  
298 regularization type and associated weights (see Table 1 for a list of recommended metadata).  
299 These metadata are stored both within the NetCDF file and in an accompanying YAML file (Ben-  
300 Kiki et al., 2009), whose hierarchical structure separates observational, forward-model, and  
301 inversion information into human- and machine-readable records of model parameters. Lastly,  
302 when available, we include the original observed geodetic fields and associated uncertainties in  
303 ASCII format as part of the model dataset. All CC data products, including NetCDF coupling values,  
304 VTU geometries, YAML metadata, and geodetic observations are freely accessible through the  
305 CC interface as well as an example Jupyter notebook that demonstrates data access, metadata  
306 parsing, and visualization.

## 307 Platform architecture

308 The CC platform operates on a virtual machine within an eight-node Proxmox virtualization  
309 cluster hosted at the Scripps Institution of Oceanography, University of California San Diego. The  
310 system is configured with two virtual CPUs and 8 GB of RAM, running AlmaLinux 9.6, with Apache  
311 serving the web application and a FastAPI backend that handles all dynamic data requests (Fig.  
312 1). The CC features two viewers: a 2D map viewer and a 3D geometry viewer. The 2D viewer  
313 displays surface-projected coupling values in a map interface and uses real-time server-side tiling  
314 via TiTiler, which converts NetCDF datasets into ``tiles'', small image segments, at multiple zoom  
315 levels that form the full map. These tiles are added as data layers in Leaflet, an open-source

316 JavaScript library that renders the interactive basemap and enables users to explore and compare  
317 coupling fields in geographic context.

318 The 3D viewer provides an interactive environment for exploring coupling fields on the original  
319 plate-interface geometry. For models where the slab depth is available, we construct 3D  
320 representations of the interface by converting geographic coordinates (latitude, longitude, and  
321 depth) to Earth-Centered Earth-Fixed coordinates and exporting the resulting surfaces as VTK  
322 PolyData (.vtp) files (Schroeder et al., 1998). The Coupling Cloud 3D viewer loads these files  
323 directly in a browser using [vtk.js](#) (Fig. 1), an open-source JavaScript library for scientific  
324 visualization. For each subduction zone, the 3D viewer includes an Earth surface layer derived  
325 from GEBCO (Becker et al., 2009), providing geographic context as users rotate, zoom, and  
326 explore coupling models, the megathrust interface and the overlying topography.

## 327 The Coupling Cloud platform

328 The CC is a browser-based workspace for finding, visualizing in 2D and 3D, comparing, and  
329 downloading published kinematic coupling models across subduction zones. Using the 2D viewer,  
330 users can select a margin from the dataset panel, display one or several models for that region,  
331 and compare their spatial distributions by toggling through layers, and adjusting the colorbar,  
332 allowing for examination of differences in the extent of coupling (Fig. 2A). In addition to the  
333 coupling fields, the CC documents supplementary fields such as uncertainty, which can become  
334 substantial where geodetic constraints are sparse, particularly in offshore regions (e.g., DeSanto  
335 et al., 2025; Lindsey et al., 2021; Nishimura et al., 2018). If provided, users can visualize these  
336 uncertainty data sets alongside the coupling maps (Fig. 2B) or download them, allowing  
337 assessment of the reliability of specific features and propagation of uncertainty into their own  
338 analyses.

339 Kinematic coupling models assume plate-interface geometries that range from planar surfaces  
340 to detailed 3D geometries, often based on the Slab2 model (Hayes et al., 2018), which may lead  
341 to variations in the inferred slip deficit distributions (Baba et al., 2002; Elston et al., 2025; Moreno  
342 et al., 2009). Within the CC 2D viewer, users can visualize and compare these geometric choices  
343 (Fig. 3C). In addition to the 2D viewer, the CC includes a 3D viewer for visualizing coupling on the  
344 3D plate-interface geometry. Users can activate the 3D viewer by selecting a subduction zone  
345 and entering its 3D view, where all models with available geometry can be explored (Fig. 3). This  
346 tool provides an intuitive way to examine how geometric assumptions influence inferred  
347 coupling, complementing the 2D surface view and enhancing comparison across models that use  
348 different representations of the plate interface. Users can download dislocation geometries as  
349 VTU files for offline visualization and analyses.

350 Variability among kinematic coupling models arises from differences in inversion setup and  
351 observational constraints (Avouac, 2015; Kaneko et al., 2010). These differences include the  
352 geodetic measurement tools used, ranging from GNSS to InSAR, leveling, paleogeodetic, and  
353 offshore measurements, as well as the time periods over which interseismic velocities are  
354 estimated and how aseismic processes such as postseismic deformation and interseismic  
355 transients are treated (Bürgmann et al., 2000; Chlieh et al., 2008; Dixon, 1991; Gagnon et al.,  
356 2005; Jackson & Bilham, 1994). The inversion strategies themselves span regularized least-  
357 squares formulations to fully Bayesian frameworks that explicitly probe the posterior  
358 distribution. Differences in regularization schemes and associated weights, fault  
359 parameterization, a priori constraints (e.g., imposed creep at depth or fixed rake), the adopted  
360 kinematic block models and plate reference frame further influence the inferred coupling  
361 distribution (Lovery et al., 2024; Métois et al., 2016; Villegas-Lanza et al., 2016).

362 These methodological differences also reflect that the quantity referred to as “kinematic  
363 coupling” is not defined identically across all studies. For example, in regions experiencing slow-  
364 slip events, some studies estimate long-term interseismic coupling, whereas others estimate  
365 coupling only during intervals between slow-slip episodes (e.g. Maubant et al., 2023; Michel et  
366 al., 2025; Radiguet et al., 2016). In classical backslip formulations (Savage, 1983), coupling is  
367 inferred by relating surface deformation to slip deficit through elastic half-space dislocation  
368 models. In contrast, viscoelastic earthquake-cycle models infer coupling using forward models  
369 that account for time-dependent viscous deformation, which can yield different coupling  
370 distributions even for the same geodetic observations. Block-model approaches derive coupling  
371 by simultaneously estimating relative block motions and slip deficit on the megathrust interface.  
372 To document such differences, we compiled metadata for each model that can be viewed directly  
373 on the platform (Fig. 4) or downloaded as YAML files. Users should consult these metadata,  
374 particularly the model type, forward-model formulation, inversion framework and other  
375 metadata (Table 1), as well as the original publications, before interpreting or comparing models.

## 376 Performance

377 We evaluate the responsiveness and scalability of the Coupling Cloud platform during interactive  
378 use, where the computational demand is highest. Initial page loads are fast, on the order of ~1  
379 second for up to about ten simultaneous users, because only a small amount of data is  
380 transferred during the initial page load. The primary computational load arises from 2D tile  
381 requests during user interaction, so we benchmark the number of concurrent requests the  
382 backend can sustain. We issue 3,000 requests for the same tile at progressively increasing  
383 concurrency levels and measure the time required for TiTiler to serve all requests. Under our  
384 current configuration, which includes two virtual CPUs and 8 GB of RAM, the total processing

385 time decreases with increasing concurrency as CPU resources are utilized more fully, until it  
386 reaches a plateau where the server is operating at maximum capacity with sustaining a  
387 throughput of approximately 45 tile requests per second (Fig. 5). A typical 2D map viewer user  
388 interaction such as panning or zooming triggers approximately 15 new tile requests. In practice,  
389 tile caching means that retrieved tiles are stored locally in the user's browser. Thus, interactions  
390 within already viewed areas impose no additional load on the backend, and the CC 2D viewer can  
391 support many more users than implied by the baseline throughput for uncached tiles.

392 Even in cases where the dynamic server becomes slow to respond due to high user load, our  
393 benchmark demonstrates that the architecture is scalable at least for small numbers of CPUs. A  
394 single-CPU configuration delivers roughly half the throughput of the two-CPU setup (Fig. 5),  
395 indicating near-linear performance scaling in this test. This suggests that adding additional CPU  
396 resources can increase system capacity, with the caveat that allocating more virtual CPUs incur  
397 higher purchasing and maintenance costs. We highlight that the 3D viewer requires no backend  
398 computation, as all visualization is handled directly in the user's browser. The only server-side  
399 operation is transferring the VTK PolyData geometry files to the client, which are typically a few  
400 megabytes in size and load within seconds, depending on the user's internet connection.

## 401 A simple demonstration: along-strike segmentation of the 402 Cascadia megathrust in kinematic coupling models

403 To illustrate the advantages of assembling many published coupling models within a single  
404 standardized framework, we present a case study for the Cascadia subduction zone. The CC  
405 currently aggregates eight full-margin Cascadia interseismic coupling models that include plate-  
406 interface depth information (Fig. 6A). These models span more than a decade of geodetic  
407 inversion studies and employ a range of elastic, viscoelastic, and boundary-based forward and  
408 inverse modeling approaches, including regularized, parameterized slip-rate deficit inversions  
409 (Schmalzle et al., 2014), regularized linear inversions (Michel et al., 2019), regularized inversions  
410 with physical constraints (Lindsey et al., 2021), Bayesian boundary inversions (Sherrill et al.,  
411 2024), and viscoelastic earthquake-cycle modeling (Pollitz & Evans, 2017; Pollitz, 2025). As a brief  
412 example of the utility of the CC platform, we view these models together (Fig. 6A1-8) to assess  
413 how their inferred coupling distributions relate to proposed along-strike segmentation of the  
414 Cascadia margin.

415 Whether a megathrust is segmented along strike controls rupture behavior and whether slip  
416 deficit is released in single margin-wide earthquakes or in a sequence of smaller events (e.g.,  
417 Arnulf et al., 2022; Bassett et al., 2025; Melnick et al., 2009; Philiposian & Meltzner, 2020).

418 Cascadia is a classic example where this question remains central (e.g., Melgar, 2021). Slow-slip  
419 and tremor catalogs reveal along-strike sections whose recurrence patterns and spatial  
420 distributions change abruptly along strike, implying structural or frictional contrasts (Bartlow,  
421 2020; Brudzinski & Allen, 2007). High-resolution seismic imaging reveals sharp changes in  
422 megathrust morphology that align with these inferred segment boundaries (Carbotte et al.,  
423 2024). Together with along-strike patterns in turbidite records, these observations have been  
424 interpreted as evidence for Cascadia's along-strike segmentation, a pattern also suggested by  
425 early geodetic coupling estimates, with higher coupling in the northern and southern segments  
426 and lower coupling in the central portion (Goldfinger et al., 2012; Schmalzle et al., 2014).

427 We define three commonly used along-strike subsections of the Cascadia margin (e.g., Ramos et  
428 al., 2021): a northern segment (Vancouver Island to  $\sim 46^\circ\text{N}$ ), a central segment ( $\sim 46\text{--}43.5^\circ\text{N}$ ), and  
429 a southern segment ( $\sim 43.5^\circ\text{N}$  to Mendocino Triple Junction). For each model, we extract Coupling  
430 Cloud-stored gridded coupling values shallower than 20 km, where along-strike variations in  
431 coupling are most commonly inferred (Fig. 6A1–2). These values correspond to spatially distinct  
432 fault patches within each along-strike segment. We describe how coupling values are distributed  
433 across these spatial units by computing a probability density function (PDF) for each model and  
434 segment (e.g., Oryan & Gabriel, 2025) using a Gaussian kernel density estimator with bandwidth  
435 selected according to Scott's rule (Scott, 2015). We note that the PDF is used as a normalized  
436 representation of the density and relative weighting of coupling values across the coupling  
437 spectrum and not as a result of repeated measurements of a stochastic process). Finally, we  
438 express each segment's PDF as a deviation from the margin-wide PDF for the same model, so  
439 that positive deviations highlight coupling values that are overrepresented within a given  
440 segment relative to the margin as a whole.

441 Our analysis shows little sensitivity to kernel bandwidth and grid resolution, and reveals that the  
442 northern-segment PDF curve rises by up to  $\sim 1$  in probability density above the margin-wide PDF  
443 at coupling values larger than 0.7. This indicates that high-coupling values are more concentrated  
444 in the northern segment than across the Cascadia subduction zone as a whole. Similarly, the  
445 central segment PDF remains below the margin-wide PDF for coupling values larger than  $\sim 0.8$ ,  
446 indicating a lower density of high-coupling values relative to the margin-wide distribution (Fig.  
447 6B2). In contrast, the southern segment does not show a higher concentration of high coupling  
448 values, and its PDF remains below the margin-wide distribution, reaching negative deviations of  
449 up to  $\sim 1$  in probability density, similar in magnitude to the positive deviations observed in the  
450 northern segment (Fig. 6B3).

451 This example averages distributions across multiple coupling models spanning a range of  
452 inversion strategies and forward-modeling approaches. These models are not strictly

453 independent, however, as they share geodetic datasets and related regularization strategies, and  
454 the ensemble spread should not be interpreted as a quantitative measure of uncertainty. Rather,  
455 the ensemble is intended to illustrate first-order behavior rather than provide a formal statistical  
456 treatment of inter-model variability and uncertainty. Even so, it shows that the concentration of  
457 coupling values in the northern and central segments aligns with previous interpretations of  
458 Cascadia's along-strike segmentation (Brudzinski & Allen, 2007; Carbotte et al., 2024; Goldfinger  
459 et al., 2012), whereas the southern segment does not exhibit a similarly coherent high-coupling  
460 pattern. This example also demonstrates how synthesizing ensemble models within the Coupling  
461 Cloud framework could help distinguish features that persist across modeling approaches from  
462 those that may depend on individual methodological choices. We therefore urge users to use the  
463 associated metadata and uncertainty information when comparing models and, most  
464 importantly, to consult the original publications describing each model, where the underlying  
465 assumptions and methodological choices are fully documented.

## 466 Current and future roles of the Coupling Cloud platform

467 The CC is designed with long-term sustainability in mind, hosted at Scripps / UC San Diego's  
468 institutional infrastructure with redundant backups and grounded in stable, widely supported  
469 data formats and libraries, ensuring continued accessibility and minimal maintenance. Our goal  
470 is for the CC to serve as a long-term community-driven global repository for kinematic coupling  
471 models, an up-to-date archive that the community can rely on for synthesis, comparison, and  
472 reproducibility. We also envision the CC to form a valuable teaching resource, offering  
473 standardized datasets for training the next generation of geodesists and subduction zone  
474 scientists, as well as providing an easy entry point for researchers new to the field. In addition,  
475 the platform is extensible and supports user-driven uploads, allowing researchers to easily  
476 contribute new coupling models, metadata, and geometries directly. We invite all authors  
477 preparing new or forthcoming coupling models to upload their datasets to the CC so that the  
478 community can benefit from timely, open, and standardized access to the latest coupling models.

479 In addition, we hope that the unified file formats adopted here, NetCDF for surface-projected  
480 coupling fields, VTU (VTK PolyData) for plate-interface dislocation geometries, and YAML for  
481 FAIR-compliant metadata, will help providing a working standard for the community. By  
482 encouraging authors to express new coupling models directly in these formats, we aim to  
483 streamline data exchange and improve reproducibility across tools and research groups. At the  
484 same time, if the community converges on alternative standards, the CC framework can readily  
485 adopt them through simple import workflows, ensuring continued support for whichever formats  
486 best serve the megathrust research community.

487 Looking ahead, we see the Coupling Cloud not only as a repository of coupling models but as an  
488 evolving platform designed to reduce methodological variability and to bridge our understanding  
489 of how slip is accumulated and released in subduction zones (e.g., Wang et al., 2012). One  
490 promising direction is to host community validated Green's functions for subduction margins  
491 (e.g., Hori et al., 2021), providing a consistent set of forward-modeling kernels that removes a  
492 major source of variability among existing coupling models (Li et al., 2015; Loverly et al., 2025;  
493 Wang et al., 2021). A near-term direction for future developments is to link coupling models more  
494 directly to the geodetic observations used in the underlying inversions. Although users can  
495 already download the coupling-model associated observational datasets, if available, future  
496 versions of the CC may place greater emphasis on graphical representation, e.g., allowing GNSS  
497 velocities and time series, InSAR displacement fields, and offshore GNSS-Acoustic measurements  
498 to be viewed alongside coupling fields.

499 Finally, seamless integration of the CC interseismic coupling archive with the SRCMOD coseismic  
500 slip repository (Mai & Thingbaijam, 2014) and the Slow Earthquake Database (Kano et al., 2018)  
501 would unify complementary perspectives on megathrust behavior. Realizing this vision would  
502 require transforming the text-based FSP (Mai, Shearer, et al., 2016) and CSV formats used by  
503 SRCMOD and Slow Earthquake Databases into the VTU and NetCDF formats adopted by the  
504 Coupling Cloud, harmonizing metadata structures across both archives, and establishing an  
505 interface that links ruptures and slow slip events to corresponding interseismic coupling models.  
506 With such integration, users could examine coseismic and slow earthquake slip distributions  
507 alongside interseismic coupling fields, offering a unified perspective on strain accumulation and  
508 release across the earthquake cycle.

## 509 Conclusions

510 We have developed the Coupling Cloud, a unified and FAIR-compliant platform for standardizing,  
511 distributing, visualizing, and comparing kinematic geodetic coupling models across global  
512 subduction zones. The CC currently hosts 96 coupling models from 55 publications covering 21  
513 subduction margins, each standardized into common file formats with preserved plate-interface  
514 geometries and complete metadata. By providing interactive 2D and 3D visualization tools and  
515 unified formats, the platform aims to remove long-standing barriers to reproducibility and to  
516 enable more transparent comparison among models constructed with differing data sets and  
517 methodologies, while associated metadata enables users to consult the original publications for  
518 methodological details. As the Coupling Cloud grows through community contributions and  
519 future integration of observational datasets and models, it is well positioned to serve as a long-  
520 lived resource for advancing understanding of megathrust deformation and seismic hazard.

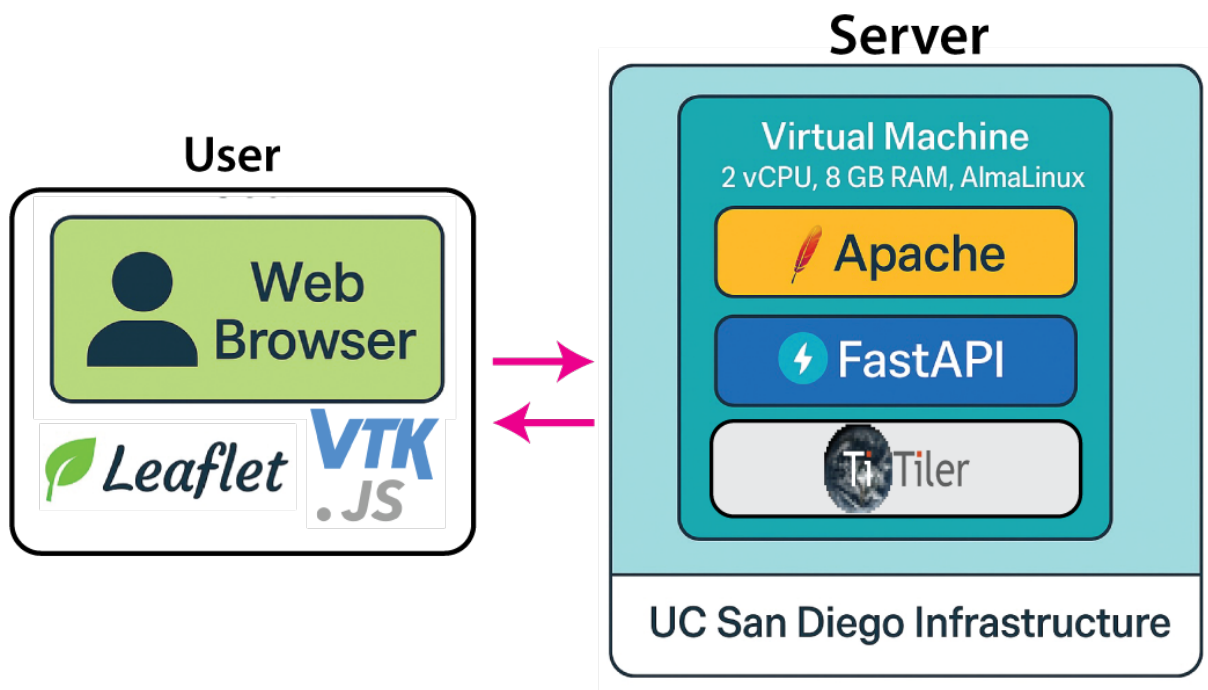
<b>Parameter</b>	<b>Description</b>
Model type	Interseismic/Inter-SSE/Block model or a combination of these.
Inversion type	Method of inversion used (e.g. Tikhonov regularization, Bayesian, stochastic Bayesian, least-squares).
Forward model formulation	Earth model used to compute surface displacement, such as a uniform elastic half-space, layered elastic structure, or a viscoelastic rheology.
Type of dislocation	Geometry of the dislocation elements (triangular, rectangular, or piecewise-linear triangular).
Number of dislocations	Total number of dislocation elements used in the forward model.
Degrees of freedom	Total number of parameters solved for in the inversion.
Type of Observations	Type(s) of geodetic observations used (e.g., Campaign GNSS, permanent GNSS, InSAR, leveling, coral etc.).
Observation Components	East/North/Up (or E/N/U)
Number of sites	Number of sites (or pixels in case of InSAR) used in the inversion.
Number of observations	Total number of individual observation components (e.g., if one site uses North/East components and another uses Up/Down, the total is 3).
Reference frame	Global geodetic reference frame (e.g., ITRF2014, ITRF2008).
Plate-fixed frame	Tectonic or plate-relative reference frame used to interpret interseismic deformation (e.g., Australian plate) including when possible.
Earliest data used	Start date of the geodetic observations incorporated in the inversion (format: YYYY or YYYY-MM or YYYY-MM-DD).
Latest data used	End date of the geodetic observations incorporated in the inversion (format: YYYY or YYYY-MM or YYYY-MM-DD).
Regularization type	Form of regularization applied during the inversion (e.g., Laplacian smoothing, Tikhonov regularization. etc.).
Smoothing weight	Value of the regularization weights used in the inversion.

Smoothing length scales	Value of length scale used in the regularization.
Couple values computed	Indicates whether coupling was computed at dislocation nodes or over full dislocation patches.
Poisson ratio	Value of the Poisson's ratio assumed if a single layer model is used.
Number of layers	Number of layers used in the model, if applicable.
Convergence model	Relative plate velocity model (required for normalization of slip deficit to obtain coupling)
Kinematic constraints	A priori assumptions about slip deficit rate (e.g., rake direction).

522

523 Table 1. Recommended metadata fields for coupling models.

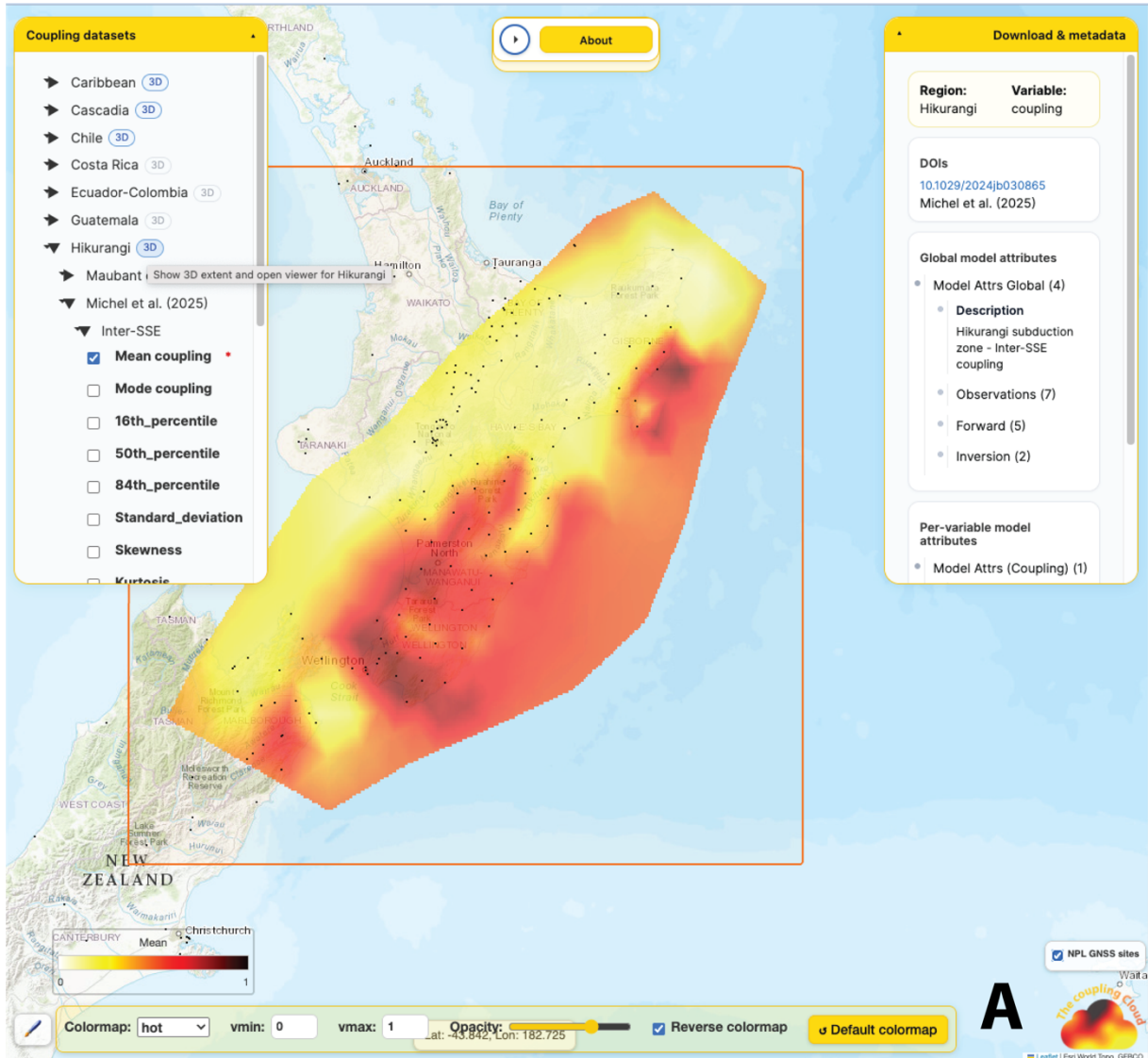
524 Figure captions



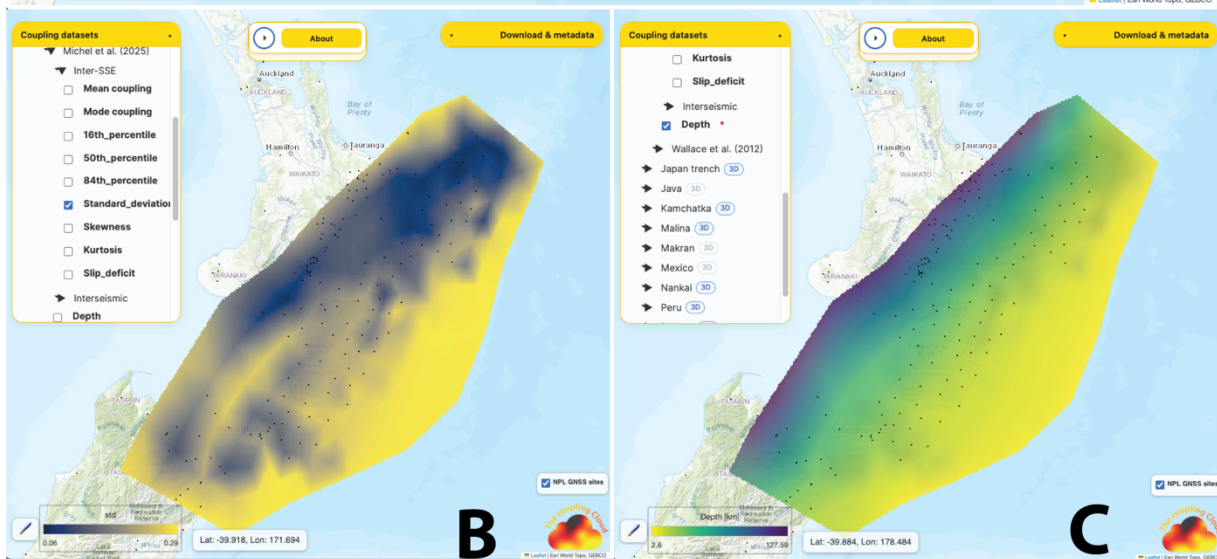
525

526 Figure 1 - CC platform architecture describing the server and user sides.

527



**A**

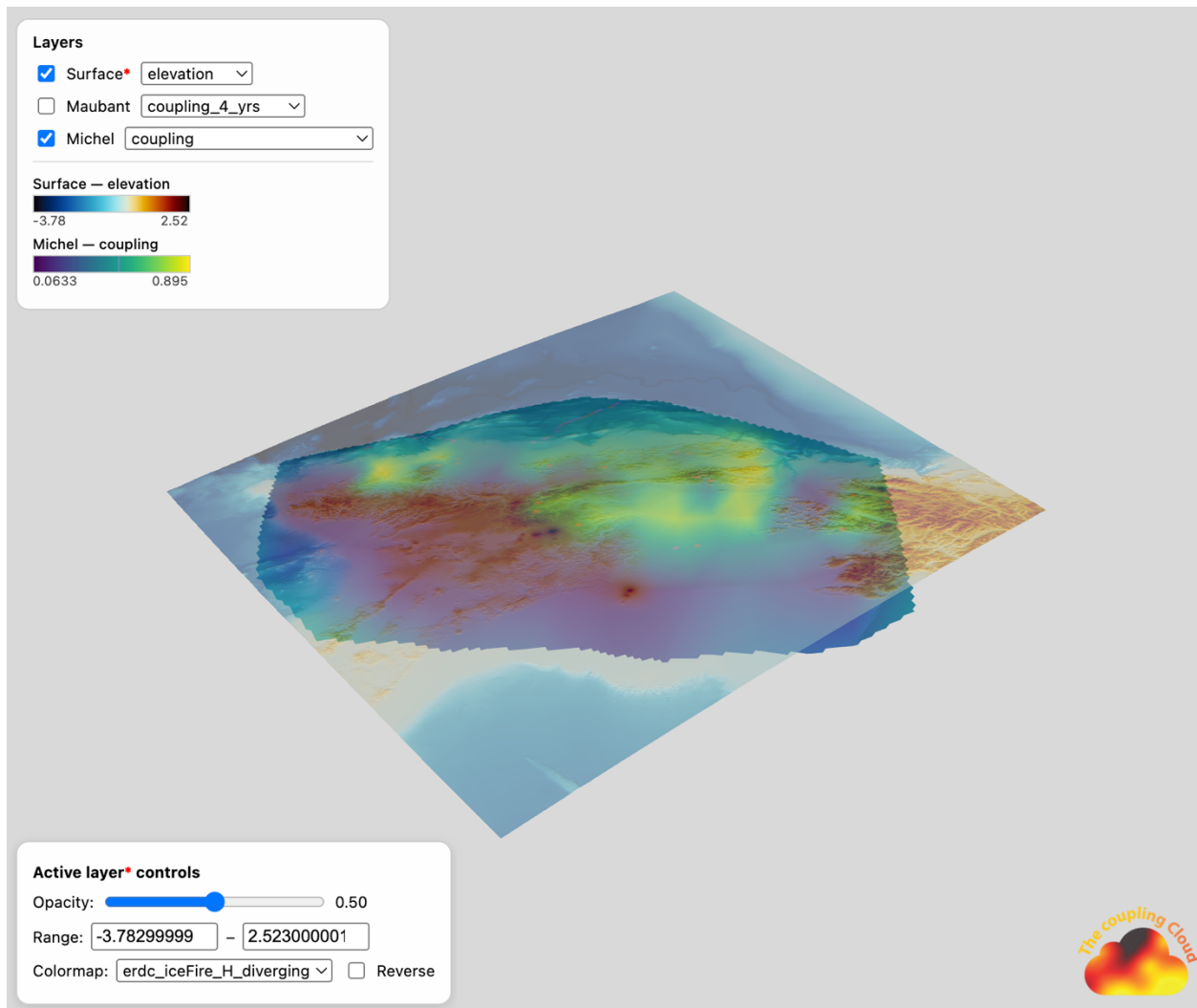


**B**

**C**

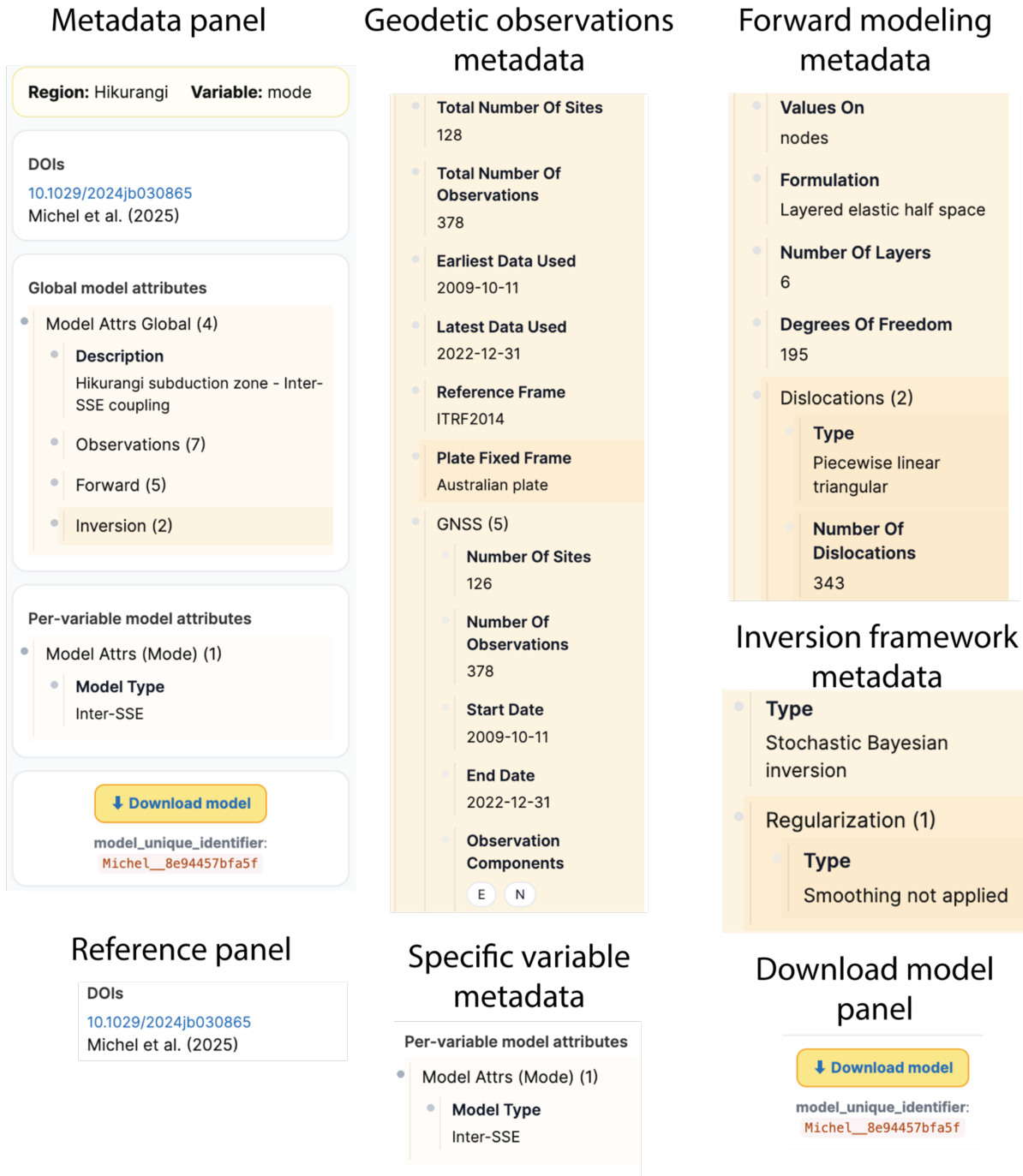
529 **Figure 2. Coupling Cloud 2D viewer overview.** The 2D viewer provides an interactive map-based  
530 interface for exploring kinematic coupling models and their associated metadata. Users can  
531 select models, adjust visualization settings, and switch seamlessly between the 2D and 3D  
532 viewers. A. The upper-left panel shows the dataset selector, which allows users to choose  
533 coupling models to display in the 2D map viewer. The 3D button switches to the 3D viewer, with  
534 the red polygon indicating the region covered by the 3D viewer. The lower-left panel contains  
535 the brush controls used to configure colormap settings. The upper-right panel displays the  
536 metadata associated with the selected coupling model, and a link to download the dataset. The  
537 “About” panel contains the full reference list and additional platform information. Black dots  
538 indicate the position of GNSS stations associated with time series in the Nevada Geodetic  
539 Laboratory (NGL). Examples showing the selection of supplementary fields, including standard  
540 deviation and interface depth, for the same coupling model in Hikurangi (Michel et al., 2025).

541



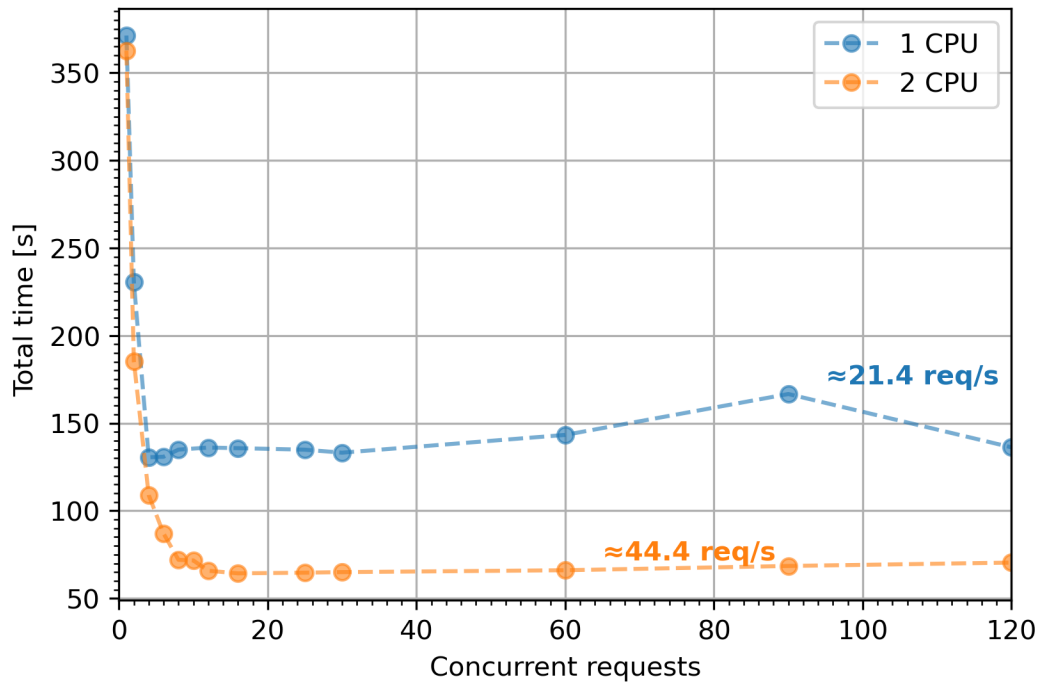
542  
 543 **Figure 3 - Coupling Cloud 3D viewer overview.** The 3D viewer enables interactive exploration of  
 544 coupling models on the actual plate-interface geometry used in each inversion. It displays the  
 545 megathrust surface in Earth-centered coordinates and overlays Earth-surface layer that provides  
 546 geographic context. Users can select which geometric or coupling layers to display and customize  
 547 their colormaps and opacity settings through the *Layers* and *Active Layers* control panels. The  
 548 example shown here is from the Hikurangi subduction zone, illustrating the coupling field for the  
 549 same model displayed in Fig 2 with the horizontal extent of the surface layer matching the red  
 550 polygon shown in Fig. 2A.

551



552  
553  
554  
555  
556  
557  
558

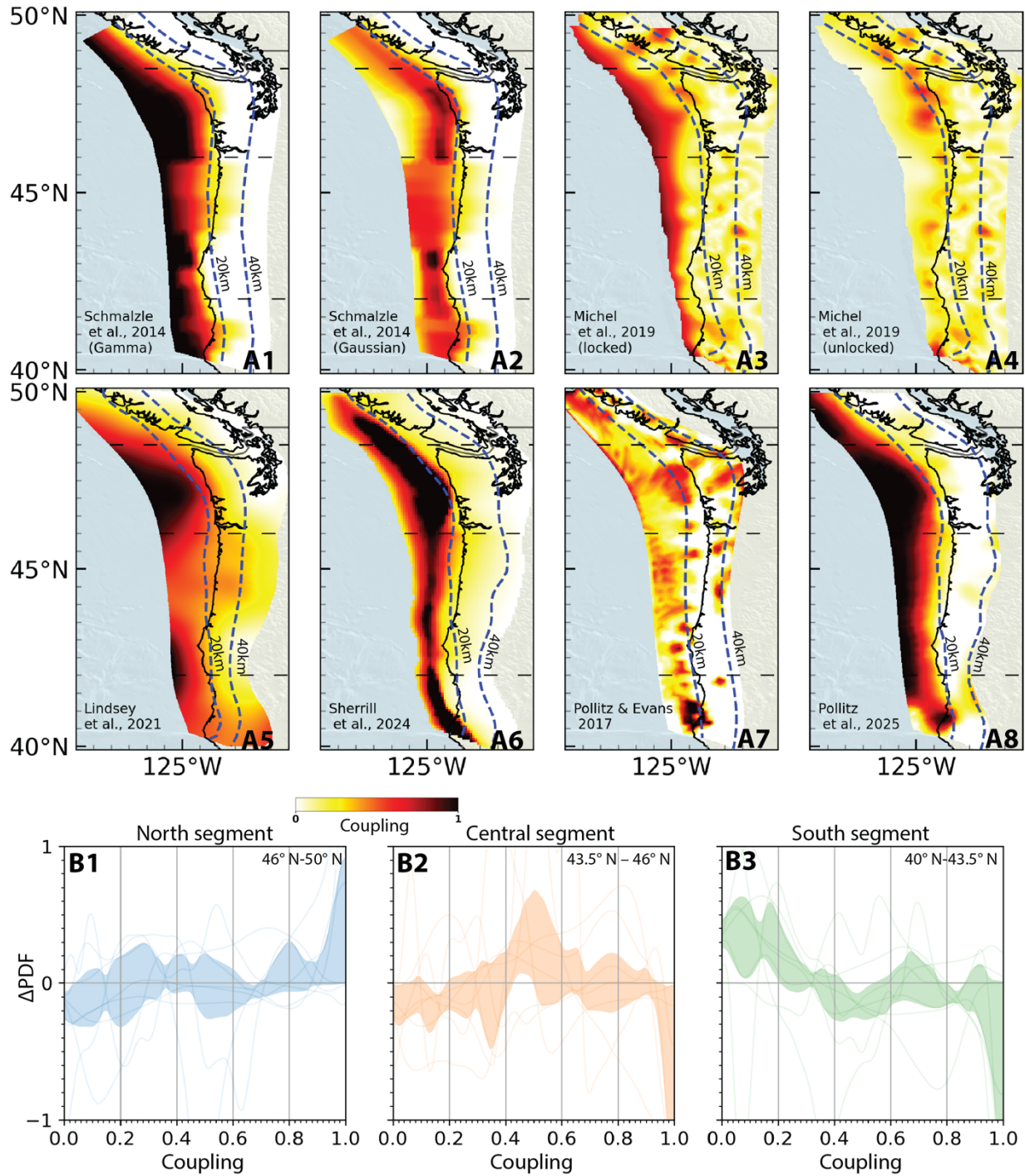
**Figure 4. Example of the metadata interface in the Coupling Cloud platform.** The metadata panel provides a detailed hierarchical summary of each coupling model, including DOIs, global attributes, per-variable attributes, observational constraints, forward-model settings, and inversion parameters. Shown here is the complete metadata for the Hikurangi coupling model of Michel et al. (2025), organized into its main components: the reference, observations, forward model, inversion, per-variable metadata, and download.



559

560 **Figure 5. Coupling Cloud backend performance benchmark showing response times for**  
 561 **increasing levels of concurrent tile requests.** Points show the total time required to process  
 562 3,000 HTTP tile requests under different CPU configurations and concurrency levels.

563



564  
 565 **Figure 6. Cascadia case study.** A - Eight Cascadia wide interseismic coupling models with slab  
 566 depth available on the CC platform (Lindsey et al., 2021; Michel et al., 2019; Pollitz & Evans, 2017;  
 567 Pollitz, 2025; Schmalzle et al., 2014; Sherrill et al., 2024), shown for interface depths shallower  
 568 than 60 km. Contours indicate the megathrust interface depth used in each model. Horizontal  
 569 dashed lines mark segments. B - Thin curves show the deviation of each model's segment-specific

570 coupling probability density from that model's margin-wide probability density ( $\Delta$ PDF). Positive  
571  $\Delta$ PDF values indicate coupling values that are more frequent within a given segment than across  
572 the margin. The shaded band denotes the 25th–75th percentile range of  $\Delta$ PDF across the eight  
573 models.

574

575

576

577

578

579

## 580 Acknowledgements

581 We thank Editor Dr. Wenbin Xu and two anonymous reviewers for their constructive feedback.  
582 We also thank Kathryn Materna, Fred Pollitz, Eileen Evans, Jean-Philippe Avouac and Adriano  
583 Gualandi for sharing their coupling models. The Coupling Cloud server was built using TiTiler  
584 (<https://github.com/developmentseed/titiler>), FastAPI (<https://github.com/fastapi/fastapi>),  
585 Leaflet (<https://leafletjs.com/>) and vtk.js (<https://kitware.github.io/vtk-js/docs/>). B.O. and A.G.  
586 acknowledges support from the IGPP Green Foundation, National Science Foundation (grant no.  
587 OAC-2311208) and CRESCENT Award 2017Y0SD. A.G. further acknowledges support from  
588 Horizon Europe (ChEESE-2P, grant number 101093038 and Geo-INQUIRE, grant number  
589 101058518) and the NSF (grant nos. OAC-2139536, EAR-2225286, EAR-2121568). E.C thanks the  
590 IGS, UNAVCO, Institut Universitaire de France and the FEDER European Community program  
591 within the Interreg Caraïbes “PREST” project. M.C. and C.D. acknowledge the Agence Nationale  
592 de la Recherche (ANR-07-BLAN-0143-01) and the IRD. B.C. and C.D. acknowledge NSF grants EAR-  
593 9526419, EAR-9804905, EAR-9909321, EAR-0510553, EAR-1114174, the University of Wisconsin-  
594 Madison and the UW-Madison Department of Geoscience Weeks endowment funds. L.D. and  
595 L.F. acknowledge Singapore Ministry of Education Tier 3b project “Investigating Volcano and  
596 Earthquake Science and Technology (InVEST)” (MOE-MOET32021-0002). A.E. acknowledges  
597 UNAVCO Graduate COCONet Fellowship and NSF grant EAR-1144418. J.T.F. acknowledges NSF  
598 grant EAR-1457361, and USGS grant G15AP00051. E.G. acknowledges the Ministry of Higher  
599 Education, Science and Technology of Indonesia (Kemendikisaintek). N.R.H. acknowledges  
600 Geospatial Information Agency of Indonesia, MEXT scholarship, Nagoya University, and Research  
601 and Innovation for Advanced Indonesia (RIIM) scheme. Y.H. acknowledges grant AS-102-SS-A09  
602 and MOST 102-2116-M-001-028-MY3. T.I. acknowledges support from the Japan Society of the  
603 Promotion of Science (JSPS) Grants-in Aid for Scientific Research (KAKENHI) grants JP21H05200  
604 and JP16H06472. J.J. acknowledges Chilean National Science Cooperation (CONICYT) through  
605 “Becas Chile” Program and MSCA Postdoctoral Fellowship (MSCA-101066069, project ERASMUS).  
606 R.J. acknowledges support from the Institut Universitaire de France and the European Research  
607 Council (ERC) under the European Union’s Horizon 2020 research and innovation program (Grant  
608 Agreement 758210 and 805256, Geo4D and iQuake projects) as well as NASA (Grant  
609 NNX16AK58G). E.K. acknowledges the French-Chilean LiA ‘Montessus de Ballore’, the Agence  
610 Nationale de la Recherche (ANR-2012-BS06-004) and the French INSU Tellus program, all data  
611 were collected by the instruments of the French mobile GNSS park GPSMob of Epos-France  
612 managed by CNRS Terre & Univers. S.M. acknowledges the ERC under the European Union’s  
613 Horizon 2020 research and innovation program (Grant 758210 for project Geo4D). S.M.  
614 acknowledges NSF award EAR-1821853. M.M. acknowledges the French-Chilean LiA “Montessus  
615 de Ballore”, CNRS, MAE, IPGP, UJF and ANR project MEGA-Chile (project number 12-BS06-004).

616 R.P. acknowledges DGAPA–UNAM PAPIIT project IA104525. E.M.S. thanks NSF grants EAR-  
617 2121631 and EAR-2045291 and USGS grant G20AP00017, and in part by Lilly Endowment, Inc.,  
618 through its support for the Indiana University Pervasive Technology Institute. J.V-L. acknowledges  
619 the Agence Nationale de la Recherche (ANR-07-BLAN-0143-01) and IRD and the Instituto  
620 Geofísico del Perú (IGP). E.O.L. acknowledges support from NSF grant OCE-2314273 and NASA  
621 (grant 80NSSC23K0654). B.L. acknowledges support from the French national space agency  
622 (CNES).A.S. acknowledges support from the ERC Consolidator grant 865963 DEEP-trigger.  
623 Instrumentation and data from OVSICORI-UNA used in this research was supported by Costa  
624 Rican Emergency Law 8933 and by Universidad Nacional de Costa Rica through the project 0097–  
625 2020 “Sistema de monitoreo geodésico (SiMoGeod) de los volcanes y de la tectónica de Costa  
626 Rica.” D.P. thanks the United States-India Educational Foundation (USIEF) for the financial  
627 support through the Fulbright-Nehru Postdoctoral Research Programme (Award 2783  
628 FNPDR/2022). L.M. acknowledges support from NASA under Grant No.~80NSSC21K0874. S.Y.  
629 acknowledges support by JSPS KAKENHI grants JP15H01140, JP16H06477 and JP21H05203, and  
630 The Project for Hazard Assessment of Large Earthquakes and Tsunamis in the Mexican Pacific  
631 Coast for Disaster Mitigation, SATREPS funded by JST-JICA (#1554361). M.R. acknowledges  
632 support by the Agence Nationale de la Recherche (ANR21-CE49-0023) SSDYN project. Y.I.  
633 acknowledges JSPS KAKENHI grant JP17J00173 and Kyoto University Foundation. T.N.  
634 acknowledges JSPS KAKENHI grants JP21H05200, JP16H06472, JP15K21755 and JP26109007. Z.  
635 L. acknowledges support from NASA’s Earth Surface and Interior Focus Area. Part of the work  
636 was carried out at the Jet Propulsion Laboratory, California Institute of Technology, under a  
637 contract with the National Aeronautics and Space Administration (80NM0018F0591). We  
638 acknowledge GNSS data from Alaska and Cascadia provided by the NSF-supported GAGE Facility  
639 (awards 1724794, 1724509).

## 640 Data and code availability

641 All coupling datasets are freely available to download from [couplingcloud.ucsd.edu](https://couplingcloud.ucsd.edu). The code to  
642 run the coupling cloud can be found in Oryan, 2025 (<https://zenodo.org/records/17821569>).

## 643 Competing interests

644 All authors declare no competing interests.

645

646 Manuscript References

647 Abe, D., & Yoshioka, S. (2022). Spatiotemporal distributions of interplate coupling in  
648 Tohoku, northeast Japan, for 14 years prior to the 2011 Tohoku-oki earthquake inverted  
649 from GNSS data. *Tectonophysics*, 838, 229479.  
650 <https://doi.org/10.1016/j.tecto.2022.229479>

651 Ahrens, J., Geveci, B., & Law, C. (2005). ParaView: An End-User Tool for Large-Data  
652 Visualization. In *Visualization Handbook* (pp. 717–731). Elsevier.  
653 <https://doi.org/10.1016/B978-012387582-2/50038-1>

654 Arnulf, A. F., Bassett, D., Harding, A. J., Kodaira, S., Nakanishi, A., & Moore, G. (2022).  
655 Upper-plate controls on subduction zone geometry, hydration and earthquake behaviour.  
656 *Nature Geoscience*, 15(2), 143–148. <https://doi.org/10.1038/s41561-021-00879-x>

657 Avouac, J.-P. (2015). From Geodetic Imaging of Seismic and Aseismic Fault Slip to Dynamic  
658 Modeling of the Seismic Cycle. *Annual Review of Earth and Planetary Sciences*, 43(Volume  
659 43, 2015), 233–271. <https://doi.org/10.1146/annurev-earth-060614-105302>

660 Baba, T., Tanioka, Y., Cummins, P. R., & Uhira, K. (2002). The slip distribution of the 1946  
661 Nankai earthquake estimated from tsunami inversion using a new plate model. *Physics of  
662 the Earth and Planetary Interiors*, 132(1–3), 59–73.

663 Bartlow, N. M. (2020). A Long-Term View of Episodic Tremor and Slip in Cascadia.  
664 *Geophysical Research Letters*, 47(3), e2019GL085303.  
665 <https://doi.org/10.1029/2019GL085303>

666 Bassett, D., Shillington, D. J., Wallace, L. M., & Elliott, J. L. (2025). Variation in slip  
667 behaviour along megathrusts controlled by multiple physical properties. *Nature*  
668 *Geoscience*, 18(1), 20–31. <https://doi.org/10.1038/s41561-024-01617-9>

669 Becker, J. J., Sandwell, D. T., Smith, W. H. F., Braud, J., Binder, B., Depner, J., et al. (2009).  
670 Global Bathymetry and Elevation Data at 30 Arc Seconds Resolution: SRTM30\_PLUS.  
671 *Marine Geodesy*, 32(4), 355–371. <https://doi.org/10.1080/01490410903297766>

672 Ben-Kiki, O., Evans, C., & Ingerson, B. (2009). Yaml ain't markup language (yaml™) version  
673 1.1. *Working Draft 2008*, 5(11).

674 Blewitt, B., Hammond, W. C., & Kreemer. (2018, September 24). Harnessing the GPS Data  
675 Explosion for Interdisciplinary Science. Retrieved October 20, 2025, from  
676 [https://eos.org/science-updates/harnessing-the-gps-data-explosion-for-](https://eos.org/science-updates/harnessing-the-gps-data-explosion-for-interdisciplinary-science)  
677 [interdisciplinary-science](https://eos.org/science-updates/harnessing-the-gps-data-explosion-for-interdisciplinary-science)

678 Brudzinski, M. R., & Allen, R. M. (2007). Segmentation in episodic tremor and slip all along  
679 Cascadia. *Geology*, 35(10), 907. <https://doi.org/10.1130/G23740A.1>

680 Burgette, R. J., Weldon, R. J., & Schmidt, D. A. (2009). Interseismic uplift rates for western  
681 Oregon and along-strike variation in locking on the Cascadia subduction zone: CASCADIA  
682 INTERSEISMIC UPLIFT AND LOCKING. *Journal of Geophysical Research: Solid Earth*,  
683 114(B1). <https://doi.org/10.1029/2008JB005679>

684 Bürgmann, R., Rosen, P. A., & Fielding, E. J. (2000). Synthetic Aperture Radar  
685 Interferometry to Measure Earth's Surface Topography and Its Deformation. *Annual*  
686 *Review of Earth and Planetary Sciences*, 28(1), 169–209.  
687 <https://doi.org/10.1146/annurev.earth.28.1.169>

688 Bürgmann, R., Kogan, M. G., Steblov, G. M., Hilley, G., Levin, V. E., & Apel, E. (2005).  
689 Interseismic coupling and asperity distribution along the Kamchatka subduction zone.  
690 *Journal of Geophysical Research: Solid Earth*, 110(B7).  
691 <https://doi.org/10.1029/2005JB003648>

692 Carbotte, S. M., Boston, B., Han, S., Shuck, B., Beeson, J., Canales, J. P., et al. (2024).  
693 Subducting plate structure and megathrust morphology from deep seismic imaging linked  
694 to earthquake rupture segmentation at Cascadia. *Science Advances*, 10(23), eadl3198.  
695 <https://doi.org/10.1126/sciadv.adl3198>

696 Cheng, G., Barnhart, W. D., & Small, D. (2024). Constraints from GPS measurements on  
697 plate coupling within the Makran subduction zone and tsunami scenarios in the western  
698 Indian Ocean. *Geophysical Journal International*, 237(1), 288–301.  
699 <https://doi.org/10.1093/gji/ggae046>

700 Chlieh, M., Avouac, J. P., Sieh, K., Natawidjaja, D. H., & Galetzka, J. (2008). Heterogeneous  
701 coupling of the Sumatran megathrust constrained by geodetic and paleogeodetic  
702 measurements. *Journal of Geophysical Research: Solid Earth*, 113(B5).  
703 <https://doi.org/10.1029/2007JB004981>

704 Chlieh, M., Beauval, C., Yepes, H., Marinière, J., Saillard, M., & Audin, L. (2021). Seismic  
705 and Aseismic Cycle of the Ecuador–Colombia Subduction Zone. *Frontiers in Earth Science*,  
706 9. <https://doi.org/10.3389/feart.2021.701720>

707 Cosenza-Murales, B., DeMets, C., Márquez-Azúa, B., Sánchez, O., Stock, J., Cabral-Cano,  
708 E., & McCaffrey, R. (2022). GPS-derived interseismic fault locking along the Jalisco–Colima  
709 segment of the Mexico subduction zone. *Geophysical Journal International*, 228(3), 2174–  
710 2197. <https://doi.org/10.1093/gji/ggab436>

711 Cruz-Atienza, V. M., Tago, J., Domínguez, L. A., Kostoglodov, V., Ito, Y., Ovando-Shelley,  
712 E., et al. (2025). Seafloor geodesy unveils seismogenesis of large subduction earthquakes  
713 in Mexico. *Science Advances*, 11(37), eadu8259. <https://doi.org/10.1126/sciadv.adu8259>

714 Dal Zilio, L., Jolivet, R., & van Dinther, Y. (2020). Segmentation of the Main Himalayan  
715 Thrust Illuminated by Bayesian Inference of Interseismic Coupling. *Geophysical Research*  
716 *Letters*, 47(4), e2019GL086424. <https://doi.org/10.1029/2019GL086424>

717 DeSanto, J. B., Schmidt, D. A., Zumberge, M., Sasagawa, G., & Chadwell, C. D. (2025). Near  
718 full locking on the shallow megathrust of the central Cascadia subduction zone revealed  
719 by GNSS-Acoustic. *Earth and Planetary Science Letters*, 665, 119463.  
720 <https://doi.org/10.1016/j.epsl.2025.119463>

721 Dixon, T. H. (1991). An introduction to the global positioning system and some geological  
722 applications. *Reviews of Geophysics*, 29(2), 249–276.  
723 <https://doi.org/10.1029/91RG00152>

724 Drooff, C., & Freymueller, J. T. (2021). New Constraints on Slip Deficit on the Aleutian  
725 Megathrust and Inflation at Mt. Veniaminof, Alaska From Repeat GPS Measurements.  
726 *Geophysical Research Letters*, 48(4), e2020GL091787.  
727 <https://doi.org/10.1029/2020GL091787>

728 Ellis, A., DeMets, C., McCaffrey, R., Briole, P., Cosenza Muralles, B., Flores, O., et al. (2019).  
729 GPS constraints on deformation in northern Central America from 1999 to 2017, Part 2:  
730 Block rotations and fault slip rates, fault locking and distributed deformation. *Geophysical*  
731 *Journal International*, 218(2), 729–754. <https://doi.org/10.1093/gji/ggz173>

732 Elston, H. M., Loveless, J. P., & Delph, J. R. (2025). Influence of Subduction Interface  
733 Geometry on Surface Displacements and Slip Processes in Cascadia. *Earth and Space*  
734 *Science*, 12(10), e2025EA004623. <https://doi.org/10.1029/2025EA004623>

735 Feigl, K. L., Agnew, D. C., Bock, Y., Dong, D., Donnellan, A., Hager, B. H., et al. (1993). Space  
736 geodetic measurement of crustal deformation in central and southern California, 1984–  
737 1992. *Journal of Geophysical Research: Solid Earth*, 98(B12), 21677–21712.  
738 <https://doi.org/10.1029/93JB02405>

739 Feng, L., Newman, A. V., Protti, M., González, V., Jiang, Y., & Dixon, T. H. (2012). Active  
740 deformation near the Nicoya Peninsula, northwestern Costa Rica, between 1996 and  
741 2010: Interseismic megathrust coupling. *Journal of Geophysical Research: Solid Earth*,  
742 117(B6). <https://doi.org/10.1029/2012JB009230>

743 Fukuda, J., & Johnson, K. M. (2008). A Fully Bayesian Inversion for Spatial Distribution of  
744 Fault Slip with Objective Smoothing. *Bulletin of the Seismological Society of America*,  
745 *98*(3), 1128–1146. <https://doi.org/10.1785/0120070194>

746 Gagnon, K., Chadwell, C. D., & Norabuena, E. (2005). Measuring the onset of locking in  
747 the Peru–Chile trench with GPS and acoustic measurements. *Nature*, *434*(7030), 205–208.  
748 <https://doi.org/10.1038/nature03412>

749 Giardini, D., Grünthal, G., Shedlock, K. M., & Zhang, P. (1999). The GSHAP Global Seismic  
750 Hazard Map. *Annals of Geophysics*, *42*(6). <https://doi.org/10.4401/ag-3784>

751 Glehman, J., Gabriel, A., Ulrich, T., Ramos, M., Huang, Y., & Lindsey, E. (2025). Partial  
752 ruptures governed by the complex interplay between geodetic slip deficit, rigidity, and  
753 pore fluid pressure in 3D Cascadia dynamic rupture simulations. *Seismica*, *2*(4).  
754 <https://doi.org/10.26443/seismica.v2i4.1427>

755 Goldberg, D. E., Koch, P., Melgar, D., Riquelme, S., & Yeck, W. L. (2022). Beyond the  
756 Teleseism: Introducing Regional Seismic and Geodetic Data into Routine USGS Finite-Fault  
757 Modeling. *Seismological Research Letters*, *93*(6), 3308–3323.  
758 <https://doi.org/10.1785/0220220047>

759 Goldfinger, C., Nelson, C. H., Morey, A. E., Johnson, J. E., Patton, J. R., Karabanov, E. B., et  
760 al. (2012). *Turbidite event history—Methods and implications for Holocene*  
761 *paleoseismicity of the Cascadia subduction zone* (No. 1661- F). *Professional Paper*. U.S.  
762 Geological Survey. <https://doi.org/10.3133/pp1661F>

763 Gombert, B., Duputel, Z., Jolivet, R., Simons, M., Jiang, J., Liang, C., et al. (2018). Strain  
764 budget of the Ecuador–Colombia subduction zone: A stochastic view. *Earth and Planetary  
765 Science Letters*, 498, 288–299. <https://doi.org/10.1016/j.epsl.2018.06.046>

766 Hanifa, N. R., Sagiya, T., Kimata, F., Efendi, J., Abidin, H. Z., & Meilano, I. (2014). Interplate  
767 coupling model off the southwestern coast of Java, Indonesia, based on continuous GPS  
768 data in 2008–2010. *Earth and Planetary Science Letters*, 401, 159–171.  
769 <https://doi.org/10.1016/j.epsl.2014.06.010>

770 Hayes, G. P. (2017). The finite, kinematic rupture properties of great-sized earthquakes  
771 since 1990. *Earth and Planetary Science Letters*, 468, 94–100.  
772 <https://doi.org/10.1016/j.epsl.2017.04.003>

773 Hayes, G. P., Moore, G. L., Portner, D. E., Hearne, M., Flamme, H., Furtney, M., & Smoczyk,  
774 G. M. (2018). Slab2, a comprehensive subduction zone geometry model. *Science*,  
775 362(6410), 58–61. <https://doi.org/10.1126/science.aat4723>

776 Hori, T., Agata, R., Ichimura, T., Fujita, K., Yamaguchi, T., & Iinuma, T. (2021). High-fidelity  
777 elastic Green’s functions for subduction zone models consistent with the global standard  
778 geodetic reference system. *Earth, Planets and Space*, 73(1), 41.  
779 <https://doi.org/10.1186/s40623-021-01370-y>

780 Hosseini, K., Matthews, K. J., Sigloch, K., Shephard, G. E., Domeier, M., & Tsekhmistrenko,  
781 M. (2018). SubMachine: Web-Based Tools for Exploring Seismic Tomography and Other

782 Models of Earth's Deep Interior. *Geochemistry, Geophysics, Geosystems*, 19(5), 1464–  
783 1483. <https://doi.org/10.1029/2018GC007431>

784 Hoyer, S., & Hamman, J. (2017). xarray: N-D labeled Arrays and Datasets in Python. *Journal*  
785 *of Open Research Software*, 5(1), 10–10. <https://doi.org/10.5334/jors.148>

786 Hsu, Y.-J., Yu, S.-B., Loveless, J. P., Bacolcol, T., Solidum, R., Luis Jr, A., et al. (2016).  
787 Interseismic deformation and moment deficit along the Manila subduction zone and the  
788 Philippine Fault system. *Journal of Geophysical Research: Solid Earth*, 121(10), 7639–  
789 7665. <https://doi.org/10.1002/2016JB013082>

790 Hunter, J. D. (2007). Matplotlib: A 2D graphics environment. *Computing in Science &*  
791 *Engineering*, 9(03), 90–95.

792 Ide, S. (2007). 4.07 - Slip Inversion. In G. Schubert (Ed.), *Treatise on Geophysics* (pp. 193–  
793 223). Amsterdam: Elsevier. <https://doi.org/10.1016/B978-044452748-6.00068-7>

794 Itoh, Y., Nishimura, T., Wang, K., & He, J. (2021). New Megathrust Locking Model for the  
795 Southern Kurile Subduction Zone Incorporating Viscoelastic Relaxation and Non-Uniform  
796 Compliance of Upper Plate. *Journal of Geophysical Research: Solid Earth*, 126(5),  
797 e2020JB019981. <https://doi.org/10.1029/2020JB019981>

798 Jackson, M., & Bilham, R. (1994). Constraints on Himalayan deformation inferred from  
799 vertical velocity fields in Nepal and Tibet. *Journal of Geophysical Research: Solid Earth*,  
800 99(B7), 13897–13912. <https://doi.org/10.1029/94JB00714>

801 Jara, J., Jolivet, R., Socquet, A., Comte, D., & Norabuena, E. (2024). Detection of slow slip  
802 events along the southern Peru - northern Chile subduction zone. *Seismica*, 3(1).  
803 <https://doi.org/10.26443/seismica.v3i1.980>

804 Jolivet, R., Simons, M., Duputel, Z., Olive, J., Bhat, H. S., & Bletery, Q. (2020). Interseismic  
805 loading of subduction megathrust drives long term uplift in northern Chile, 1–21.  
806 <https://doi.org/10.1029/2019GL085377>

807 Kaneko, Y., Avouac, J.-P., & Lapusta, N. (2010). Towards inferring earthquake patterns  
808 from geodetic observations of interseismic coupling. *Nature Geoscience*, 3(5), 363–369.  
809 <https://doi.org/10.1038/ngeo843>

810 Kano, M., Aso, N., Matsuzawa, T., Ide, S., Annoura, S., Arai, R., et al. (2018). Development  
811 of a Slow Earthquake Database. *Seismological Research Letters*, 89(4), 1566–1575.  
812 <https://doi.org/10.1785/0220180021>

813 Kano, M., Ikeuchi, A., Nishimura, T., Miyazaki, S., & Matsushima, T. (2021). Potential of  
814 megathrust earthquakes along the southern Ryukyu Trench inferred from GNSS data.  
815 *Earth, Planets and Space*, 73(1), 199. <https://doi.org/10.1186/s40623-021-01531-z>

816 Klein, E., Métois, M., Meneses, G., Vigny, C., & Delorme, A. (2018). Bridging the gap  
817 between North and Central Chile: insight from new GPS data on coupling complexities  
818 and the Andean sliver motion. *Geophysical Journal International*, 213(3), 1924–1933.  
819 <https://doi.org/10.1093/gji/ggy094>

820 Laske, G., Masters, G., Ma, Z., & Pasyanos, M. (2013). Update on CRUST1.0 - A 1-degree  
821 Global Model of Earth's Crust. In *Geophys. Res. Abstract*.

822 Li, Shanshan, & Freymueller, J. T. (2018). Spatial Variation of Slip Behavior Beneath the  
823 Alaska Peninsula Along Alaska-Aleutian Subduction Zone. *Geophysical Research Letters*,  
824 45(8), 3453–3460. <https://doi.org/10.1002/2017GL076761>

825 Li, Shaoyang, Moreno, M., Bedford, J., Rosenau, M., & Oncken, O. (2015). Revisiting  
826 viscoelastic effects on interseismic deformation and locking degree: A case study of the  
827 Peru-North Chile subduction zone. *Journal of Geophysical Research: Solid Earth*, 120(6),  
828 4522–4538. <https://doi.org/10.1002/2015JB011903>

829 Li, Shaoyang, Wang, K., Wang, Y., Jiang, Y., & Dosso, S. E. (2018). Geodetically Inferred  
830 Locking State of the Cascadia Megathrust Based on a Viscoelastic Earth Model. *Journal of*  
831 *Geophysical Research: Solid Earth*, 123(9), 8056–8072.  
832 <https://doi.org/10.1029/2018JB015620>

833 Lindsey, E. O., Mallick, R., Hubbard, J. A., Bradley, K. E., Almeida, R. V., Moore, J. D. P., et  
834 al. (2021). Slip rate deficit and earthquake potential on shallow megathrusts. *Nature*  
835 *Geoscience*, 14(5), 321–326. <https://doi.org/10.1038/s41561-021-00736-x>

836 Lindsey, E. O., Wang, Y., Aung, L. T., Chong, J.-H., Qiu, Q., Mallick, R., et al. (2023). Active  
837 subduction and strain partitioning in western Myanmar revealed by a dense survey GNSS  
838 network. *Earth and Planetary Science Letters*, 622, 118384.  
839 <https://doi.org/10.1016/j.epsl.2023.118384>

840 Liu, Z., Owen, S., Dong, D., Lundgren, P., Webb, F., Hetland, E., & Simons, M. (2010).  
841 Estimation of interplate coupling in the Nankai trough, Japan using GPS data from 1996  
842 to 2006. *Geophysical Journal International*. [https://doi.org/10.1111/j.1365-](https://doi.org/10.1111/j.1365-246X.2010.04600.x)  
843 [246X.2010.04600.x](https://doi.org/10.1111/j.1365-246X.2010.04600.x)

844 Loveless, J. P., & Meade, B. J. (2016). Two decades of spatiotemporal variations in  
845 subduction zone coupling offshore Japan. *Earth and Planetary Science Letters*, *436*, 19–  
846 30. <https://doi.org/10.1016/j.epsl.2015.12.033>

847 Lovery, B., Chlieh, M., Norabuena, E., Villegas-Lanza, J. C., Radiguet, M., Cotte, N., et al.  
848 (2024). Heterogeneous Locking and Earthquake Potential on the South Peru Megathrust  
849 From Dense GNSS Network. *Journal of Geophysical Research: Solid Earth*, *129*(2),  
850 e2023JB027114. <https://doi.org/10.1029/2023JB027114>

851 Lovery, B., Radiguet, M., Chlieh, M., Norabuena, E., Villegas-Lanza, J. C., Cresseaux, J., et  
852 al. (2025). Viscoelastic Relaxation Following the 2001 Mw 8.4 Arequipa Earthquake and  
853 Its Impact on the Interseismic Coupling of the South Peru Megathrust. *Geophysical*  
854 *Research Letters*, *52*(12), e2024GL113879. <https://doi.org/10.1029/2024GL113879>

855 Luo, H., Wang, K., Feng, L., & Hill, E. M. (2025). Interseismic secondary zone of subsidence  
856 during earthquake cycles in subduction zones. *Nature Geoscience*, *18*(10), 1027–1033.  
857 <https://doi.org/10.1038/s41561-025-01778-1>

858 Mai, Shearer, P., Ampuero, J., & Lay, T. (2016). Standards for Documenting Finite-Fault  
859 Earthquake Rupture Models. *Seismological Research Letters*, 87(3), 712–718.  
860 <https://doi.org/10.1785/0220150204>

861 Mai, P. M., & Thingbaijam, K. K. S. (2014). SRCMOD: An Online Database of Finite-Fault  
862 Rupture Models. *Seismological Research Letters*, 85(6), 1348–1357.  
863 <https://doi.org/10.1785/0220140077>

864 Mai, P. M., Schorlemmer, D., Page, M., Ampuero, J., Asano, K., Causse, M., et al. (2016).  
865 The Earthquake-Source Inversion Validation (SIV) Project. *Seismological Research Letters*,  
866 87(3), 690–708. <https://doi.org/10.1785/0220150231>

867 Materna, K., Murray, J. R., Pollitz, F., & Patton, J. R. (2023). Slip Deficit Rates on Southern  
868 Cascadia Faults Resolved with Viscoelastic Earthquake Cycle Modeling of Geodetic  
869 Deformation. *Bulletin of the Seismological Society of America*, 113(6), 2505–2518.  
870 <https://doi.org/10.1785/0120230007>

871 Maubant, L., Frank, W. B., Wallace, L. M., Williams, C. A., & Hamling, I. (2023). Imaging  
872 the Spatiotemporal Evolution of Plate Coupling With Interferometric Radar (InSAR) in the  
873 Hikurangi Subduction Zone. *Geophysical Research Letters*, 50(19), e2023GL105388.  
874 <https://doi.org/10.1029/2023GL105388>

875 Maubant, Louise, Radiguet, M., Pathier, E., Doin, M.-P., Cotte, N., Kazachkina, E., &  
876 Kostoglodov, V. (2022). Interseismic coupling along the Mexican subduction zone seen by

877 InSAR and GNSS. *Earth and Planetary Science Letters*, 586, 117534.  
878 <https://doi.org/10.1016/j.epsl.2022.117534>

879 Meade, B. J. (2007). Algorithms for the calculation of exact displacements, strains, and  
880 stresses for triangular dislocation elements in a uniform elastic half space. *Computers &*  
881 *Geosciences*, 33(8), 1064–1075. <https://doi.org/10.1016/j.cageo.2006.12.003>

882 Melgar, D. (2021). Was the January 26th, 1700 Cascadia Earthquake Part of a Rupture  
883 Sequence? *Journal of Geophysical Research: Solid Earth*, 126(10), e2021JB021822.  
884 <https://doi.org/10.1029/2021JB021822>

885 Melnick, D., Bookhagen, B., Strecker, M. R., & Echtler, H. P. (2009). Segmentation of  
886 megathrust rupture zones from fore-arc deformation patterns over hundreds to millions  
887 of years, Arauco peninsula, Chile. *Journal of Geophysical Research: Solid Earth*, 114(B1).  
888 <https://doi.org/10.1029/2008JB005788>

889 Métois, M., Socquet, A., & Vigny, C. (2012). Interseismic coupling, segmentation and  
890 mechanical behavior of the central Chile subduction zone. *Journal of Geophysical*  
891 *Research: Solid Earth*, 117(B3). <https://doi.org/10.1029/2011JB008736>

892 Métois, M., Socquet, A., Vigny, C., Carrizo, D., Peyrat, S., Delorme, A., et al. (2013).  
893 Revisiting the North Chile seismic gap segmentation using GPS-derived interseismic  
894 coupling. *Geophysical Journal International*, 194(3), 1283–1294.  
895 <https://doi.org/10.1093/gji/ggt183>

896 Métois, M., Vigny, C., & Socquet, A. (2016). Interseismic Coupling, Megathrust  
897 Earthquakes and Seismic Swarms Along the Chilean Subduction Zone (38°–18°S). *Pure and*  
898 *Applied Geophysics*, 173(5), 1431–1449. <https://doi.org/10.1007/s00024-016-1280-5>

899 Michel, S., Gualandi, A., & Avouac, J.-P. (2019). Interseismic Coupling and Slow Slip Events  
900 on the Cascadia Megathrust. *Pure and Applied Geophysics*, 176(9), 3867–3891.  
901 <https://doi.org/10.1007/s00024-018-1991-x>

902 Michel, S., Jolivet, R., Klein, E., & Maubant, L. (2025). 14 Years of Slip on the Hikurangi  
903 Subduction Zone. *Journal of Geophysical Research: Solid Earth*, 130(7), e2024JB030865.  
904 <https://doi.org/10.1029/2024JB030865>

905 Minson, S. E., Simons, M., & Beck, J. L. (2013). Bayesian inversion for finite fault  
906 earthquake source models I—theory and algorithm. *Geophysical Journal International*,  
907 194(3), 1701–1726. <https://doi.org/10.1093/gji/ggt180>

908 Moreno, M. S., Bolte, J., Klotz, J., & Melnick, D. (2009). Impact of megathrust geometry  
909 on inversion of coseismic slip from geodetic data: Application to the 1960 Chile  
910 earthquake. *Geophysical Research Letters*, 36(16).  
911 <https://doi.org/10.1029/2009GL039276>

912 Nishimura, T., Yokota, Y., Tadokoro, K., & Ochi, T. (2018). Strain partitioning and interplate  
913 coupling along the northern margin of the Philippine Sea plate, estimated from Global  
914 Navigation Satellite System and Global Positioning System-Acoustic data. *Geosphere*,  
915 14(2), 535–551. <https://doi.org/10.1130/GES01529.1>

916 Noda, A., Saito, T., & Fukuyama, E. (2018). Slip-Deficit Rate Distribution Along the Nankai  
917 Trough, Southwest Japan, With Elastic Lithosphere and Viscoelastic Asthenosphere.  
918 *Journal of Geophysical Research: Solid Earth*, 123(9), 8125–8142.  
919 <https://doi.org/10.1029/2018JB015515>

920 Okada, Y. (1985). Surface deformation due to shear and tensile faults in a half-space.  
921 *International Journal of Rock Mechanics and Mining Sciences & Geomechanics Abstracts*,  
922 23(4), 128. [https://doi.org/10.1016/0148-9062\(86\)90674-1](https://doi.org/10.1016/0148-9062(86)90674-1)

923 Okada, Y. (1992). Internal deformation due to shear and tensile faults in a half-space.  
924 *Bulletin - Seismological Society of America*.

925 Oryan, B. (2025, December 4). Code for the coupling cloud. Zenodo. Retrieved from  
926 <https://zenodo.org/records/17821569>

927 Panda, D., & Lindsey, E. O. (2024). Overriding Plate Deformation Controls Inferences of  
928 Interseismic Coupling Along the Himalayan Megathrust. *Journal of Geophysical Research:*  
929 *Solid Earth*, 129(9), e2024JB029819. <https://doi.org/10.1029/2024JB029819>

930 Perry, M., Muller, C., Protti, M., Feng, L., & Hill, E. M. (2025). Interseismic Megathrust  
931 Coupling at the Osa Peninsula, Costa Rica. *Journal of Geophysical Research: Solid Earth*,  
932 130(7), e2024JB030641. <https://doi.org/10.1029/2024JB030641>

933 Philibosian, B., & Meltzner, A. J. (2020). Segmentation and supercycles: A catalog of  
934 earthquake rupture patterns from the Sumatran Sunda Megathrust and other well-

935 studied faults worldwide. *Quaternary Science Reviews*, 241, 106390.  
936 <https://doi.org/10.1016/j.quascirev.2020.106390>

937 Plata-Martinez, R., Iinuma, T., Tomita, F., Nakamura, Y., Nishimura, T., & Hori, T. (2024).  
938 Revisiting Slip Deficit Rates and Its Insights Into Large and Slow Earthquakes at the Nankai  
939 Subduction Zone. *Journal of Geophysical Research: Solid Earth*, 129(12), e2023JB027942.  
940 <https://doi.org/10.1029/2023JB027942>

941 Pollitz, F.F., & Evans, E. L. (2017). Implications of the earthquake cycle for inferring fault  
942 locking on the Cascadia megathrust. *Geophysical Journal International*, 209(1), 167–185.  
943 <https://doi.org/10.1093/gji/ggx009>

944 Pollitz, Fred F. (1997). Gravitational viscoelastic postseismic relaxation on a layered  
945 spherical Earth. *Journal of Geophysical Research: Solid Earth*, 102(B8), 17921–17941.  
946 <https://doi.org/10.1029/97JB01277>

947 Pollitz, Fred F. (2025). 3D Viscoelastic Models of Slip-Deficit Rate Along the Cascadia  
948 Subduction Zone. *Journal of Geophysical Research: Solid Earth*, 130(1), e2024JB029847.  
949 <https://doi.org/10.1029/2024JB029847>

950 Radiguet, M., Perfettini, H., Cotte, N., Gualandi, A., Valette, B., Kostoglodov, V., et al.  
951 (2016). Triggering of the 2014 Mw7.3 Papanoa earthquake by a slow slip event in  
952 Guerrero, Mexico. *Nature Geoscience*, 9(11), 829–833.  
953 <https://doi.org/10.1038/ngeo2817>

954 Ramos, M. D., Huang, Y., Ulrich, T., Li, D., Gabriel, A.-A., & Thomas, A. M. (2021). Assessing  
955 Margin-Wide Rupture Behaviors Along the Cascadia Megathrust With 3-D Dynamic  
956 Rupture Simulations. *Journal of Geophysical Research: Solid Earth*, 126(7),  
957 e2021JB022005. <https://doi.org/10.1029/2021JB022005>

958 Rew, R., & Davis, G. (1990). NetCDF: an interface for scientific data access. *IEEE Computer  
959 Graphics and Applications*, 10(4), 76–82. <https://doi.org/10.1109/38.56302>

960 van Rijnsingen, E. M., Calais, E., Jolivet, R., Robertson, R., & Ryan, G. A. (2021). Inferring  
961 Interseismic Coupling Along the Lesser Antilles Arc: A Bayesian Approach. *Journal of  
962 Geophysical Research*, 21.

963 Rousset, B., Lasserre, C., Cubas, N., Graham, S., Radiguet, M., DeMets, C., et al. (2016).  
964 Lateral Variations of Interplate Coupling along the Mexican Subduction Interface:  
965 Relationships with Long-Term Morphology and Fault Zone Mechanical Properties. *Pure  
966 and Applied Geophysics*, 173(10), 3467–3486. [https://doi.org/10.1007/s00024-015-1215-  
967 6](https://doi.org/10.1007/s00024-015-1215-6)

968 Savage, J. C. (1983). A dislocation model of strain accumulation and release at a  
969 subduction zone. *Journal of Geophysical Research*.  
970 <https://doi.org/10.1029/JB088iB06p04984>

971 Schlömer, N. (2022). meshio: Tools for mesh files. *GitHub Repository*.

972 Schmalzle, G. M., McCaffrey, R., & Creager, K. C. (2014). Central Cascadia subduction zone  
973 creep. *Geochemistry, Geophysics, Geosystems*, 15(4), 1515–1532.  
974 <https://doi.org/10.1002/2013GC005172>

975 Schroeder, W., Martin, K. M., & Lorensen, W. E. (1998). *The visualization toolkit (2nd ed.):*  
976 *an object-oriented approach to 3D graphics*. USA: Prentice-Hall, Inc.

977 Sherrill, E. M., Johnson, K. M., & Jackson, N. M. (2024). Locating Boundaries Between  
978 Locked and Creeping Regions at Nankai and Cascadia Subduction Zones. *Journal of*  
979 *Geophysical Research: Solid Earth*, 129(10), e2024JB029346.  
980 <https://doi.org/10.1029/2024JB029346>

981 Small, D. T., & Melgar, D. (2021). Geodetic Coupling Models as Constraints on Stochastic  
982 Earthquake Ruptures: An Example Application to PTHA in Cascadia. *Journal of Geophysical*  
983 *Research: Solid Earth*, 126(7), e2020JB021149. <https://doi.org/10.1029/2020JB021149>

984 Stevens, V. L., & Avouac, J. P. (2015). Interseismic coupling on the main Himalayan thrust.  
985 *Geophysical Research Letters*, 42(14), 5828–5837.  
986 <https://doi.org/10.1002/2015GL064845>

987 Sullivan, C., & Kaszynski, A. (2019). PyVista: 3D plotting and mesh analysis through a  
988 streamlined interface for the Visualization Toolkit (VTK). *Journal of Open Source Software*,  
989 4(37), 1450. <https://doi.org/10.21105/joss.01450>

990 Tarantola, A. (2005). *Inverse Problem Theory and Methods for Model Parameter*  
991 *Estimation*. Society for Industrial and Applied Mathematics.  
992 <https://doi.org/10.1137/1.9780898717921>

993 Tarantola, A., & Valette, B. (1982). Generalized nonlinear inverse problems solved using  
994 the least squares criterion. *Reviews of Geophysics*, 20(2), 219–232.  
995 <https://doi.org/10.1029/RG020i002p00219>

996 Tomita, F., Inuma, T., Agata, R., & Hori, T. (2021). Development of a Trans-Dimensional  
997 Fault Slip Inversion for Geodetic Data. *Journal of Geophysical Research: Solid Earth*,  
998 126(5), e2020JB020991. <https://doi.org/10.1029/2020JB020991>

999 Tsang, L. L. H., Meltzner, A. J., Hill, E. M., Freymueller, J. T., & Sieh, K. (2015). A  
1000 paleogeodetic record of variable interseismic rates and megathrust coupling at Simeulue  
1001 Island, Sumatra. *Geophysical Research Letters*, 42(24), 10,585-10,594.  
1002 <https://doi.org/10.1002/2015GL066366>

1003 Villegas-Lanza, J. C., Chlieh, M., Cavalié, O., Tavera, H., Baby, P., Chire-Chira, J., & Nocquet,  
1004 J.-M. (2016). Active tectonics of Peru: Heterogeneous interseismic coupling along the  
1005 Nazca megathrust, rigid motion of the Peruvian Sliver, and Subandean shortening  
1006 accommodation. *Journal of Geophysical Research: Solid Earth*, 121(10), 7371–7394.  
1007 <https://doi.org/10.1002/2016JB013080>

1008 Wallace, L. M., Barnes, P., Beavan, J., Van Dissen, R., Litchfield, N., Mountjoy, J., et al.  
1009 (2012). The kinematics of a transition from subduction to strike-slip: An example from the

1010 central New Zealand plate boundary. *Journal of Geophysical Research: Solid Earth*,  
1011 117(B2). <https://doi.org/10.1029/2011JB008640>

1012 Wang, K., & Dixon, T. (2004). "Coupling" Semantics and science in earthquake research.  
1013 *Eos, Transactions American Geophysical Union*, 85(18), 180–180.  
1014 <https://doi.org/10.1029/2004EO180005>

1015 Wang, K., Hu, Y., & He, J. (2012). Deformation cycles of subduction earthquakes in a  
1016 viscoelastic Earth. *Nature*, 484(7394), 327–332. <https://doi.org/10.1038/nature11032>

1017 Wang, K., Zhu, Y., Nissen, E., & Shen, Z.-K. (2021). On the Relevance of Geodetic  
1018 Deformation Rates to Earthquake Potential. *Geophysical Research Letters*, 48(11),  
1019 e2021GL093231. <https://doi.org/10.1029/2021GL093231>

1020 Wang, L., Hainzl, S., & Mai, P. M. (2015). Quantifying slip balance in the earthquake cycle:  
1021 Coseismic slip model constrained by interseismic coupling. *Journal of Geophysical*  
1022 *Research: Solid Earth*, 120(12), 8383–8403. <https://doi.org/10.1002/2015JB011987>

1023 Wang, Z. (2011). Seismic Hazard Assessment: Issues and Alternatives. *Pure and Applied*  
1024 *Geophysics*, 168(1), 11–25. <https://doi.org/10.1007/s00024-010-0148-3>

1025 Wessel, P., Luis, J. F., Uieda, L., Scharroo, R., Wobbe, F., Smith, W. H. F., & Tian, D. (2019).  
1026 The Generic Mapping Tools Version 6. *Geochemistry, Geophysics, Geosystems*, 20(11),  
1027 5556–5564. <https://doi.org/10.1029/2019GC008515>

1028 Widiyantoro, S., Gunawan, E., Muhari, A., Rawlinson, N., Mori, J., Hanifa, N. R., et al.  
1029 (2020). Implications for megathrust earthquakes and tsunamis from seismic gaps south  
1030 of Java Indonesia. *Scientific Reports*, 10(1), 15274. [https://doi.org/10.1038/s41598-020-](https://doi.org/10.1038/s41598-020-72142-z)  
1031 72142-z

1032 Wilkinson, M. D., Dumontier, M., Aalbersberg, Ij. J., Appleton, G., Axton, M., Baak, A., et  
1033 al. (2016). The FAIR Guiding Principles for scientific data management and stewardship.  
1034 *Scientific Data*, 3(1), 160018. <https://doi.org/10.1038/sdata.2016.18>

1035 Xue, L., Schwartz, S., Liu, Z., & Feng, L. (2015). Interseismic megathrust coupling beneath  
1036 the Nicoya Peninsula, Costa Rica, from the joint inversion of InSAR and GPS data. *Journal*  
1037 *of Geophysical Research: Solid Earth*, 120(5), 3707–3722.  
1038 <https://doi.org/10.1002/2014JB011844>

1039 Yabuki, T., & Matsu'ura, M. (1992). Geodetic data inversion using a Bayesian information  
1040 criterion for spatial distribution of fault slip. *Geophysical Journal International*, 109(2),  
1041 363–375. <https://doi.org/10.1111/j.1365-246X.1992.tb00102.x>

1042 Yokota, Y., Ishikawa, T., Watanabe, S., Tashiro, T., & Asada, A. (2016). Seafloor geodetic  
1043 constraints on interplate coupling of the Nankai Trough megathrust zone. *Nature*,  
1044 534(7607), 374–377. <https://doi.org/10.1038/nature17632>

1045

1046